UNIVERSIDAD DE INVESTIGACIÓN DE TECNOLOGÍA EXPERIMENTAL YACHAY

Escuela de Ciencias Físicas y Nanotecnología

TÍTULO: Solving the Atomic Structure of ultra-thin CaF_2 layers on the Si(100) surface

Trabajo de integración curricular presentado como requisito para
la obtención
del título de Físico

Autor:

Joshua Mateo Salazar Mejía

Tutor:

Ph.D. Henry Pinto

Urcuquí, Julio 2020

Urcuquí, 9 de junio de 2020

SECRETARÍA GENERAL
(Vicerrectorado Académico/Cancillería)
ESCUELA DE CIENCIAS FÍSICAS Y NANOTECNOLOGÍA
CARRERA DE FÍSICA
ACTA DE DEFENSA No. UITEY-PHY-2020-00011-AD

A los 9 días del mes de junio de 2020, a las 16:30 horas, de manera virtual mediante videoconferencia, y ante el Tribunal Calificador, integrado por los docentes:

Presidente Tribunal de Defensa	Dra. PERALTA ARCIA, MAYRA ALEJANDRA DE JESUS , Ph.D.
Miembro No Tutor	Dr. VACACELA GOMEZ, CRISTIAN ISAAC , Ph.D.
Tutor	Dr. PINTO ESPARZA, HENRY PAUL , Ph.D.

El(la) señor(ita) estudiante **SALAZAR MEJIA, JOSHUA MATEO**, con cédula de identidad No. **1725159410**, de la **ESCUELA DE CIENCIAS FÍSICAS Y NANOTECNOLOGÍA**, de la Carrera de **FÍSICA**, aprobada por el Consejo de Educación Superior (CES), mediante Resolución **RPC-SO-39-No.456-2014**, realiza a través de videoconferencia, la sustentación de su trabajo de titulación denominado: **SOLVING THE ATOMIC STRUCTURE OF ULTRA-THIN CaF2 LAYERS ON THE Si(100) SURFACE** , previa a la obtención del título de **FÍSICO/A**.

El citado trabajo de titulación, fue debidamente aprobado por el(los) docente(s):

Tutor	Dr. PINTO ESPARZA, HENRY PAUL , Ph.D.

Y recibió las observaciones de los otros miembros del Tribunal Calificador, las mismas que han sido incorporadas por el(la) estudiante.

Previamente cumplidos los requisitos legales y reglamentarios, el trabajo de titulación fue sustentado por el(la) estudiante y examinado por los miembros del Tribunal Calificador. Escuchada la sustentación del trabajo de titulación a través de videoconferencia, que integró la exposición de el(la) estudiante sobre el contenido de la misma y las preguntas formuladas por los miembros del Tribunal, se califica la sustentación del trabajo de titulación con las siguientes calificaciones:

Tipo	Docente	Calificación
Presidente Tribunal De Defensa	Dra. PERALTA ARCIA, MAYRA ALEJANDRA DE JESUS , Ph.D.	10,0
Tutor	Dr. PINTO ESPARZA, HENRY PAUL , Ph.D.	10,0
Miembro Tribunal De Defensa	Dr. VACACELA GOMEZ, CRISTIAN ISAAC , Ph.D.	10,0

Lo que da un promedio de: **10 (Diez punto Cero)**, sobre 10 (diez), equivalente a: **APROBADO**

Para constancia de lo actuado, firman los miembros del Tribunal Calificador, el/la estudiante y el/la secretario ad-hoc.

Certifico que *en cumplimiento del Decreto Ejecutivo 1017 de 16 de marzo de 2020, la defensa de trabajo de titulación (o examen de grado modalidad teórico práctica) se realizó vía virtual, por lo que las firmas de los miembros del Tribunal de Defensa de Grado, constan en forma digital.*

SALAZAR MEJIA, JOSHUA MATEO
Estudiante

Dra. PERALTA ARCIA, MAYRA ALEJANDRA DE JESUS , Ph.D.
Presidente Tribunal de Defensa

Firmado electrónicamente por:
MAYRA ALEJANDRA DE
JESUS PERALTA ARCIA

Dr. PINTO ESPARZA, HENRY PAUL , Ph.D.
Tutor

Firmado electrónicamente por:
HENRY PAUL PINTO

Dr. VACACELA GOMEZ, CRISTIAN ISAAC , Ph.D.
Miembro No Tutor

Firmado electrónicamente por:
CRISTIAN ISAAC VACACELA GOMEZ

CIFUENTES TAFUR, EVELYN CAROLINA
Secretario Ad-hoc

Firmado electrónicamente por:
EVELYN CAROLINA CIFUENTES TAFUR

AUTORÍA

Yo, **Joshua Mateo Salazar Mejía**, con cédula de identidad 1725159410, declaro que las ideas, juicios, valoraciones, interpretaciones, consultas bibliográficas, definiciones y conceptualizaciones expuestas en el presente trabajo; así cómo, los procedimientos y herramientas utilizadas en la investigación, son de absoluta responsabilidad de el/la autora (a) del trabajo de integración curricular. Así mismo, me acojo a los reglamentos internos de la Universidad de Investigación de Tecnología Experimental Yachay.

Urcuquí, Julio de 2020.

Joshua Mateo Salazar Mejía
CI:1715159410

AUTORIZACIÓN DE PUBLICACIÓN

Yo, **Joshua Mateo Salazar Mejía,** con cédula de identidad 1725159410, cedo a la Universidad de Investigación de Tecnología Experimental Yachay, los derechos de publicación de la presente obra, sin que deba haber un reconocimiento económico por este concepto. Declaro además que el texto del presente trabajo de titulación no podrá ser cedido a ninguna empresa editorial para su publicación u otros fines, sin contar previamente con la autorización escrita de la Universidad.

Asimismo, autorizo a la Universidad que realice la digitalización y publicación de este trabajo de integración curricular en el repositorio virtual, de conformidad a lo dispuesto en el Art. 144 de la Ley Orgánica de Educación Superior

Urcuquí, Julio 2020.

Joshua Mateo Salazar Mejía
CI:1725159410

Acknowledgements

Un listado de agradecimiento adecuado sería una lista infinita que agregar aquí, pero dadas las circunstancias puedo "truncar la expansión" para demostrar mi agradecimiento a quienes más han influído durante el estudio de mi carrera científica y elaboración de este trabajo.

Primero, a mis padres: Jorge Salazar y Janneth Mejía, quienes cultivaron mi curiosidad, alimentarion mi avidez por aprender y motivaron tantos de esos varios impulsos aventureros que me han llevado a visitar tantos lugares a repartir y expandir mis conocimientos.

A Abigail Morales, por brindarme apoyo incondicional con todos mis problemas, incluso sin pedir su ayuda, y recordárme el por qué vale la pena esforzarme, en esos momentos que menos fuerzas me quedaban.

A mis primos Sebastián Constante y Diego Ruiz por sus profundas discusiones filosóficas, preguntas que me han invitado a ver el mundo desde diferentes perspectivas y desear saber más para responderlas.

A mis amigos, Juan Diego Pillajo y Jenner Feijoó por ser esa clase de amigos que te levantan el ánimo por más enfadado (¡incluso con ellos mismo!) o desmotivado te encuentres, aunque especialmente por jamás negarse a sacrificar su tiempo por una altruista aventura a divulgar ciencia en algún lugar recóndito del Ecuador.

A mis abuelas Magdalena Auz y Rosa Rodriguez, por brindarme tanto amor y fuerza para perseguir mis sueños, cuidando de mi y velando por mi bienestar.

A mi tutor, Henry Pinto, por compartirme un poco de sus superpoderes para investigar y hacer ciencia, pero sobre todo por ser un gran amigo e inspirador maestro.

También al staff detrás del Supercomputador Quinde I, que hicieron posibles varios cálculos presentados en este trabajo. Y finalmente, un agradecimiento especial a todos esos héroes anónimos de Wikipedia, que hicieron más fluído el leer y aprender sobre millones de temas variados durante mi carrera.

Abstract

El desarrollo de la electrónica molecular requiere la efectiva manipulación de una molécula sobre su sustrato, y también una manipulación precisa a escala atómica[1]. En el siguiente trabajo se estudiará la interfaz de CaF_2/Si(100) que actualmente es usada para la manipulación electrónica de moléculas a escala nanométrica. Esta interfaz ha sido construida experimentalmente hasta cierto régimen de recubrimiento[2,3]. Desafortunadamente, hasta donde sabemos, una descripción acertada de la formación en forma de franjas de la interfaz de CaF_2/Si(100) sigue sin resolverse[3]. Para resolver este inconveniente proponemos un estudio teórico de esta interfaz usando la teoría del funcional de la densidad (Density funtional Theory, DFT) para obtener la configuración electrónica y estructura atómica más probable de la interfaz. Las aproximaciones de gradiente generalizado tienden a fallar al describir las energías de cohesión entre las capas de este tipo de sistemas. Para simularlos adecuadamente es necesario tomar en cuenta las interacciones débiles de van der Waals que surgen entre el CaF2 y la superficie de Si(100). En este trabajo se emplearán fucionales de densidad que usen van der Waals[4] para investigar la configuración y energías de varias interfaces. Además sus respectivas energías, imágenes de STM simuladas de las estructuras con más estabilidad serán generadas y comparadas directamente con experimentos.

Palabras clave: DFT, vdW-DF, optb86-vdW, VASP, STM.

Abstract

Molecular electronics development requires the effective electronic isolation of a given molecule with the substrate as well as a precise atomic manipulation[1]. In this work, we study the CaF_2/Si(100) interface that it is currently used for electronic manipulation of molecules at the nanoscale. This interface has been already grown experimentally for certain coverage regime[2,3]. Unfortunately, to the best of our knowledge, an accurate description of the stripe formation of CaF_2/Si(100) interface remains unsolved[3]. In order to solve this problem, we propose a theoretical study of this interface using density-functional theory (DFT) to obtain the electronic structure and the most likely atomic configurations of the interface. The generalized gradient approximation functionals tend to fail when describing the correct cohesive energies between the layers in this kind of systems. To accurately simulate such systems it is needed to take into account the weak van der Waals interactions arising between the CaF_2 and the Si(100) surface. In this work, we will use a van der Waals density functional (vdW-DF) approach[4]. Employing this functional, we investigate the configuration and energetics of several interfaces, the simulated scanning tunneling microscopy (STM) images of the most stable interfaces will be generated and compared directly with the experiment.

Keywords: DFT, vdW-DF, optb86-vdW, VASP, STM.

Contents

List of Figures **x**

List of Tables **xii**

List of Papers **xiii**

1 Introduction **1**

1.1 Problem Statement 2

1.1.1 Exact atomic structure of CaF_2/Si(100) stripe interface 3

1.2 General and Specific Objectives 3

1.3 Outline 3

2 Theoretical Background **5**

2.1 Schrödinger equation for many body systems 5

2.2 Solid state physics approximations 6

2.2.1 The Born-Oppenheimer approximation 7

2.2.2 Crystal lattice periodicity 7

2.2.2.1 Bloch's theorem 9

2.2.2.2 Plane wave expansion 10

2.2.3 Pseudopotentials 10

2.2.4 The Projector Augmented Wave (PAW) method 11

2.3 Principles of Density Functional Theory 12

2.3.1 The Hohenberg-Kohn theorem 12

2.3.2 Kohn-Sham equations 13

2.3.3 The Exchange and Correlation Functionals 15

2.3.3.1 The Local Density Approximation (LDA) 15

2.3.3.2 The Generalized Gradient Approximation(GGA) 16

2.3.3.3 The optb86-vdW functional 16

2.4 Electron Microscopy 17

2.4.1 Scanning Tunneling Microscopy . . . 18
    2.4.1.1 Line-scan STM mode . . . 18
    2.4.1.2 Density of States . . . 19
2.5 Simulation Software . . . 20
    2.5.1 VASP: Vienna Ab initio Simulation Package . . . 20
    2.5.2 ASE: Atomic Simulation Environment . . . 21
2.6 The CaF_2/Si(100) interface . . . 21
    2.6.1 The Si(100) surface . . . 22
    2.6.2 Electronic and structural properties of fcc Si and Si(100). . . . 23
    2.6.3 Chemical Vapor Deposition of CaF_2 on Si(100) . . . 25

3 Methodology **27**
3.1 Structural relaxation . . . 28
    3.1.1 Optimal parameters for bulk silicon crystal . . . 28
    3.1.2 Si(100)-(1×1) and Si(100)-(2×1) surfaces . . . 31
    3.1.3 The CaF_2/Si(100) interface . . . 32
        3.1.3.1 The wetting layer . . . 33
        3.1.3.2 The stripe structure . . . 34

4 Results & Discussion **37**
4.1 Electronic structure . . . 37
    4.1.1 Bulk silicon . . . 38
    4.1.2 Si(100) 1×1, 2×1 and 2×2 surfaces . . . 38
    4.1.3 The CaF_2/Si(100) 3×2 wetting layer . . . 39
        4.1.3.1 STM simulation . . . 41
    4.1.4 The CaF_2/Si(100) 3×4 wetting layer . . . 43
    4.1.5 Solving the stripe structure . . . 43
        4.1.5.1 The S1 stripe structure . . . 45
        4.1.5.2 The S2 stripe structure . . . 46
        4.1.5.3 S2 model that solve the observed stripe topology . . . 48

5 Conclusions & Outlook **49**

A Short Appendix 1 Heading for the Table of Contents **51**

Bibliography **55**

List of Figures

2.1 Scanning Tunneling Microscope schematic . . . 18
2.2 Line-scan STM for measuring surface topographies . . . 19
2.3 Si(100) surface reconstruction and buckling . . . 23
2.4 Silicon band gap . . . 24
2.5 Si(100) band structure . . . 25

3.1 Bulk Silicon unit cell . . . 28
3.2 Cut off energy convergence . . . 28
3.3 *k*-points mesh energy convergence . . . 29
3.4 Equation of state of bulk silicon . . . 30
3.5 Si(100) 2×1 surface . . . 31
3.6 $CaF2_2$/Si(100) wetting layer . . . 32
3.7 $CaF2_2$/Si(100) wetting layer experimental STM images . . . 33
3.8 Different possible wetting layer configurations . . . 34
3.9 STM-stripe . . . 34
3.10 Stripe a-s1 type . . . 35
3.11 Stripe a-s2 type . . . 36

4.1 Bulk silicon DoS . . . 38
4.2 Si(100) 1×1 2×1 DoS . . . 39
4.3 $CaF2_2$/Si(100) 3x4 wetting layer a-type . . . 40
4.4 STM at positive bias voltage . . . 41
4.5 STM at negative bias voltage . . . 42
4.6 $CaF2_2$/Si(100) wetting layer computed STM images . . . 43
4.7 Experimentally measured band gaps . . . 44
4.8 PDOS of the CaF_2 stripe a-s1 type . . . 46
4.9 PDOS of the CaF_2 stripe a-s2 type . . . 47
4.10 $CaF2_2$ stripe computed STM images . . . 48

A.1 $CaF2_2$/Si(100) 3x4 wetting layer b-type 52
A.2 $CaF2_2$/Si(100) 3x4 wetting layer c-type 53
A.3 $CaF2_2$/Si(100) 3×4 wetting layer d-type 54

List of Tables

2.1 Table of physical properties of silicon 24

3.1 Fitting coefficients for the bulk silicon equation of state 30
3.2 Crystallographic data for fcc-Si 31

4.1 Table of convergence parameters and relevant values 37
4.2 Table with all wetting layer types total energies 45
4.3 Band gap values 48

List of Papers

[1] Enumerated list of published and submitted papers which for portions of the thesis.

Chapter 1

Introduction

Human technology development is limited by the quality and physicochemical properties of materials. Along our early ancient history, human ages have been mainly described by the materials we dominated: Stone Age, starting with the control of fire and just limited to the craft of stone tools; Copper Age, the point in which we discovered metalworking, letting us to harness the ability to smelt and design a wider range of tools; Bronze Age, where alloys were understood, hence promoting the features of their currently available metals; and later, the Iron Age, marking a big jump of technological progress linked to the discovery of iron smelting processes and carbon steel production. Mass production of steel-made weapons and tools determine this time epoch, due to the mechanical superiority agains other metals, such as bronze. Also, there was a technological boost motivated by the objective of further improving the quality of the steel alloys. Then, many improved and complex designs for furnaces for iron and steel metalworking were designed along this age, many focused on better regulating the carbon-iron ratio and removal of impurities[5].

Slightly greater strength vs other tools and weapons was decisive at those times, sharper scythes would allow farmers to cut through more hay without getting exhausted too quickly, and harder weapons would become critical against less developed technologies. Even a those times, nanotechnology became a game changer in the steel alloys fields. Damascus steel is a great example of how nanostructures greatly improve the physical and mechanical properties of materials. The ancient exact process of Damascus steel metalworking is not known yet, remaining as a mystery of how it was achievable with the technology at that time. It is speculated that the formation of nanotubes within the steel alloy is related to an special process of carburizing reactions involving the burned biomass in the furnaces[6]. Even though modern steel alloys outperform the features of Damascus swords, for those times there were very famous because of their strength. But the process of how and why was not figured out until the early years of this millenium, the now known presence of carbon nanowires, nanotubes and iron carbide compounds within the alloy[7].

If the exact structure would be have known, it could have boosted further the technological advancements relating that type of material. Nowadays, the science and technology development gives us powerful tools to manipulate and understand the structure of materials as never before. In this context, the research on fields of materials science really shape the future technological developments by giving us more powerful and efficient materials to construct with. The optimal way for deducing materials features would be a bottom-up technique, and this can be done by solving the atomic structure of the materials.

The studied interface in this thesis has been subject of active research within the scientific community in the last decades due to its interesting properties and potential applications to the development of molecular electronics, multiple solid state devices, and even soft-error free memory storing devices[8]. Specially due to its easiness and feasibility of industrial production: high quality silicon layer preparation is a well known and developed process in nowadays semiconductors industry, and also, high purity epitaxially grown CaF_2 layers on top of silicon wafers are relatively easy to achieve via Chemical Vapor Deposition (CVD)[2], Molecular Beam Epitaxy (MBE)[9] and many other experimental techniques, (specially on top of the Si(111) surfaces).

Nevertheless, the studies of the formation of CaF_2 ultra-thin layers on top of Si(100) surface is still not well understood. High quality epitaxial films of CaF_2 are found to be good candidates for the design of this kind of novel microelectronic and optoelectronic devices[10] for using it as a barrier layer in field-effect transistors and resonant tunneling diodes[8], with a band gap large enough to isolate the electronic interactions coming out from the silicon layers in the ultra-thin film growth on top of them.

1.1 Problem Statement

Optical microscope methods do not have enough magnifying power to let us probe the atomic structure of materials. Even by electron microscope techniques, the most powerful imaging techniques nowadays, getting clear information about the atomic positions of a sample may be still challenging. Hence, for probing the spatial structure of surfaces one can rely on techniques such as transmission electron microscope (TEM), serial-section electron microscope (ssEM), scanning prove microscopy (SPM), electron energy loss spectroscopy (EELS), ion scattering spectroscopy (ISS) and low energy electron diffraction (LEED), to name some of them[11].

In this thesis, we will be focused on scanning tunneling microscope (STM) studies on CaF_2/Si(100) interface. Given the working principles of such type of measurement, the collected information from the sample will give us information about the spatial distribution of the occupied/unoccupied electronic states of the sample, but not details about the exact positions of the atoms at the interface. Considering current technology, it is experimentally very challenging to get the exact positions of atoms in a surface sample. The data obtained from multiple experimental approaches should be processed and analyzed to get an approximate picture of the exact positions of the atoms. Computational studies have become very handy by allowing a reverse method of solution for this kind of research problems. With this approach, the objective of this study is to propose possible atomic configurations and predict the STM images. Density-functional theory plays a major role by giving us a set of tools for performing such computational studies. Previously reported studies reconstructed similar wetting layer topographies as the the experimental data demonstrated, but it did not take into account for the van der Waals interactions that may contribute to the physisorbed species interactions.

1.1.1 Exact atomic structure of CaF_2/Si(100) stripe interface

The exact atomic structure of the CaF_2/Si(100) stripe interface remains to be unsolved[3]. Despite the formation mechanism of the CaF_2/Si(111) is well reported, the mechanisms of the formation process at the nanoscale of the wetting layer over the Si(100) are not fully understood[12], but many different possible chemical etching reactions involving CaF_2 acting on top of pure Si surfaces are proposed in the literature[2]. It has been found that the interface morphologies strongly deppend on the surface orientation ({100} or {111}) and temperature of the epitaxial growth process[10]. This is mostly caused by the higher energies of formation of the calcium difluorite CaF_2 crystal on the (100) direction rather than in (111). Therefore, the coverage is found to be less uniform versus the Si(111) surface[10]. Nevertheless, the multiple combinations in which the reactions may occur and also the different sites of chemisorption and physisorption of the molecular CaF_2 motivate us from resolving the exact atomic structure of the interface.

The experimentally obtained low temperature STM images at different voltages give us an approximate picture of the surface atomic structure and its topography. Depending on the negative or positive voltages of operation, one can probe the spatial distribution of the occupied and unnoccupied electronic states, respectively. But still, exact atomic positions cannot be resolved precisely because the spacial distribution of orbitals are the ones being measured, not the position of the nuclei at the interface. It is here where DFT can play a key role in solving with high accuracy the actual position of the atoms constituting the interface.

1.2 General and Specific Objectives

The overall objective of this work is to perform a computational study of the atomic and electronic structure of the CaF_2/Si(100) interface using DFT. To take in account for the van der Waals interactions that may arise from the physisorbed species at the surface, van der Waals density functional (vdW-DF) will be used; this will improve the predictions calculations reported in the scientific literature. For investigating the atomic structure, we aim to calculate the most stable configuration of the observed periodic 3×4 supercell of the wetting layer arising from the first steps of deposition of CaF_2 of the studied interface. Then, to calculate constant-current mode of the STM images at different voltages and compare them with experimental data. Finally, to compute line-scans of the surface topography for comparing the computed structure with respect to the experiment. The same approach is repeated in order to find an accurate atomic description of the CaF_2 stripe-like structures found to form on top of the initial wetting layers.

1.3 Outline

This work is split into five main chapters, giving detail of the performed calculations and the physical/mathematical principles behind them. The first chapter, this Introduction, briefly described the relevance and active research behind the unsolved atomic structure of the CaF_2/Si(100) interface and how it is expected to have interesting properties for the design of new molecular electronics technologies.

The second one, Theoretical Background, illustrates the DFT theory and how it is constructed from the Hohenberg-Kohn theorem and Kohn-Sham equations. Also it will explain some of the approximations applied over the computational process in order for us to be able to converge to an estimate and, at the same time, reliable answer.

The third chapter is the Methodology, where we review the properties of the studied structures and give details about the calculation and choice of the optimal parameters used to perform the computational simulations.

The Results and Discussion chapter will address the analysis of the computed STM images and scrutiny of the obtained electronic structure of the interface.

And finally, in the Conclusions and Outlook chapter we will wrap up the results and deepen into the discussion for giving an insight of the further research needed on this topic.

Chapter 2

Theoretical Background

2.1 Schrödinger equation for many body systems

In order to understand the underlying physics of the simulations we are performing, we should remember that all the physical properties of solids are given by their electronic structure[13]. Electrons are half integer spin particles, so their statistical properties are given by the Fermi-Dirac distribution, and its motion inside materials are governed by the laws of quantum mechanics.

The Schrödinger equation, equation 2.1, describes the motion of a quantum mechanical particle

$$\hat{H}\psi = \hat{E}\psi \tag{2.1}$$

where its Hamiltonian $H = \hat{T} + \hat{V}$ which details the system and contains information about the potential $\hat{V}$ (deppending on the nature of the system) and kinetic ($\hat{T} = -\frac{\hbar^2}{2m}\nabla^2$) energy of it[14]. The energy operator is given by $\hat{E} = i\hbar\partial/\partial t$, so eqn. 2.1 becomes:

$$\left[-\frac{\hbar^2}{2m}\nabla^2 + \hat{V}\right]\psi(\mathbf{r}, t) = \hat{E}\psi(\mathbf{r}, t) = i\hbar\frac{\partial}{\partial t}\psi(\mathbf{r}, t) \tag{2.2}$$

The wavefunction depends in the vector $\mathbf{r}$, where the coordinates for electrons are represented by a lowercase $\vec{r}_i$, nuclei with an uppercase $\vec{R}_I$, being the the indices $i \in [1, N]$, $I \in [1, M]$ for the number electrons and nuclei in our system.

$$\mathbf{r} = \left\{\left(\overrightarrow{r}_1, s_1,\right), \ldots, \left(\overrightarrow{r}_N, s_N\right); \left(\overrightarrow{R}_1, s_1\right),, \ldots, \left(\overrightarrow{R}_M, s_M\right)\right\} \tag{2.3}$$

From the set of wavefuntions and eigenvalues of this differential equation all physical observables can be addressed and computed[15]. This linear partial differential equation can be separated into its temporal part using the energy eigenvalue E of the equation 2.4. The form of the separated solutions is described by the following infinite linear combination:

$$\psi(\mathbf{r},t) = \sum_{i=0}^{\infty} c_i \psi_i(\mathbf{r})\, e^{-iE_i t/\hbar} \tag{2.4}$$

The ground state configuration (lowest energy state) of the system will be given by $\psi_0(\mathbf{r})$ and the simultaneous probability of finding electron 1, electron 2... and electron N at position $\vec{r}_1$, $\vec{r}_2$, $\vec{r}_N$ respectively can be computed from: $|\psi_0(\mathbf{r})|^2$ [16].

Since we are dealing with many atoms system, the potential operator $\hat{V}$ is composed of the following interactions: electron-electron $\hat{V}_{e-e}$, electron-nuclei V_{e-n}, and nuclei-nuclei interactions $\hat{V}_{n-n}$.

$$\begin{aligned}
\hat{V} &= \hat{V}_{e-e} + \hat{V}_{e-n} + \hat{V}_{n-n} && (2.5)\\
&= +\frac{1}{2}\sum_{i\neq j}\frac{e^2}{4\pi\varepsilon_0}\frac{1}{\left|r_i - r_j\right|} && (2.6)\\
&\quad -\frac{1}{2}\sum_{i,I}\frac{e^2}{4\pi\varepsilon_0}\frac{Z_i}{|r_i - R_I|} && (2.7)\\
&\quad +\frac{1}{2}\sum_{I\neq J}\frac{e^2}{4\pi\varepsilon_0}\frac{Z_I Z_J}{|R_I - R_J|} && (2.8)\\
& && (2.9)
\end{aligned}$$

Therefore, using those expressions for the potential and kinetic energies, the full Schrödinger equation becomes:

$$\left[-\sum_i \frac{\hbar^2}{2m_e}\nabla_i^2 - \sum_I \frac{\hbar^2}{2M_I}\nabla_I^2 + \frac{1}{2}\sum_{i\neq j}\frac{e^2}{4\pi\varepsilon_0}\frac{1}{\left|r_i - r_j\right|} - \frac{1}{2}\sum_{i,I}\frac{e^2}{4\pi\varepsilon_0}\frac{Z_i}{|r_i - R_I|} + \frac{1}{2}\sum_{I\neq J}\frac{e^2}{4\pi\varepsilon_0}\frac{Z_I Z_J}{|R_I - R_J|}\right]\psi(\mathbf{r},t) = E_{total}\psi(\mathbf{r},t) \tag{2.10}$$

2.2 Solid state physics approximations

Solving exactly the Schrödinger equation 2.4 for a system with higher complexity than the hydrogen atom is impossible due to the increasing amount of electronic coordinates and the many-body nature of the problem [13].

Therefore, multiple approximations and conventions may be used to address the problem of solving this many-body equation [17] and getting information about the wavefunctions composing the particles inside the studied solid. Considerations such as: the high nuclei-electron mass ratio, use of periodic solutions due to the periodic boundary conditions in regular solids, finding symmetries, setting cutoff limits to the infinite sums, and using perturbation theory can also greatly boost the speed of the calculations and considerably reduce the computational hurdle.

2.2.1 The Born-Oppenheimer approximation

Considering the time scaling of the interactions and motion of the nuclei in the lattice versus the electrons moving around them, the events relating the atomic nucleus occur in longer times than those relating the electrons. This is due to the fact the mass of the proton is three order of magnitude heavier than the electrons[18]. Therefore their interactions may be decoupled via the adiabatic theorem of quantum mechanics. The adiabatic approximation will keep the instantaneous ground state positions of the electrons while as the nuclei move. Therefore, the energy minimization process for the electronic part can be solved simultaneously, along with the motion of the nuclei in the lattice[19].

Considering the Schrödinger equation with nuclear coordinates given by $\vec{R}_i$ and electronic positions by $\vec{r}$, being s the index running through the coupled atomic wavefunctions and i the indices of the nuclei, then we can write:

$$\widehat{H}\psi_s\left(\vec{r},\vec{R}\right) = E_s\psi_s\left(\vec{r},\vec{R}\right) \tag{2.11}$$

The degrees of freedom can be decoupled into the electronic wavefunctions of each atom, given by ψ_i, and the electron-nuclear states, described as χ_{si}. Those coupled states deppend on the positions of the atoms and are coefficients of the pure electronic wavefunctions.

$$\psi_s\left(\vec{r},\vec{R}\right) = \sum_i \chi_{si}\left(\vec{R}\right)\psi_i\left(\vec{r}\right), \tag{2.12}$$

For getting analytical expressions for the electron-nuclear states, we can combine equations 2.11 and 2.12, integrate them with respect to the electronic coordinates to obtain:

$$\left[-\frac{1}{2}\left(\sum_j \nabla_j^2/M_j\right) + E_i\left(\vec{R}\right) - E_s\right]\chi_{si}\left(\vec{R}\right) = -\sum_{i'} C_{ii'}\chi_{si}\left(\vec{R}\right) \tag{2.13}$$

Where the coefficient is given by $C_{ii'} = A_{ii'} + B_{ii'}$, and the terms are given by:

$$A_{ii'}\left(\vec{R}\right) = \sum_J \frac{1}{M_j}\left\langle\psi_i\left(R\right)|\nabla_J|\psi_{i'}\left(\vec{R}\right)\right\rangle\nabla_j \quad , \quad B_{ii'}\left(\vec{R}\right) = \sum_J \frac{1}{2M_j}\left\langle\psi_i\left(R\right)|\nabla_J^2|\psi_{i'}\left(\vec{R}\right)\right\rangle \tag{2.14}$$

The adiabatic approximation comes here, where we ignore the $C_{ii'}$ off-diagonal terms in order to assume the electrons do not move with respect of the motion of the nucleus. Even though the electronic $\psi_i(\vec{r})$ wavefunctions get a change in energy, the electrons remain in the same state, and there is no energy transfer between the electronic degrees of freedom, as equation 2.13 just deppends on nuclear coordinates $\vec{R}$[20].

2.2.2 Crystal lattice periodicity

A crystalline structure, ideally, displays perfect periodicity over all spatial coordinates in a microscopic scale[21]. By applying a proper translation given by multiples of the lattice constant describing the crystal over a coordinate in one specific direction, returns the same structure, given its periodic boundary conditions. Mathematically, this can be written as follows:

$$f\left(r + T\left(n_1, n_2, n_3, \ldots\right)\right) = f\left(r\right) \tag{2.15}$$

$$\vec{T}\left(\vec{n}\right) \equiv T\left(n_1 n_2 \ldots\right) = n_1 \vec{a}_1 + n_2 \vec{a}_2 + \ldots \tag{2.16}$$

With the index $i = 1, \ldots d$ running up to a spatial dimension d and the vector $\vec{n} = (n_1, n_2, n, \ldots n_d)$ containing indices relating the number of periodic translations applied over each direction i with lattice vector $\vec{a}_i$. In reciprocal space, the reciprocal vectors are given by the expression and related with the Kroenecker delta δ_{ij} (valued 1 if $i = j$, 0 otherwise):

$$\vec{b}_i = \frac{2\pi}{\Omega_{cel1}} \left(\vec{a}_j \times \vec{a}_k\right) \varepsilon_{ijk} \qquad , \qquad \vec{a}_i \times \vec{b}_j = 2\pi \delta_{ij} \tag{2.17}$$

Given the periodicity of the function at equation 2.15, a Fourier transformation may be applied for wavevectors $\vec{q}$ defined in reciprocal space. The construction of expressions for Fourier components becomes simplier if we constrain the number of components to be limited to a finite discrete value enclosed inside the whole crystal volume $\Omega_{crystal}$ containing $N_{cells} = \{N_i\} = N_1 \times N_2 \times ...$, where N_i describe the number of cells along each dimension.

$$e^{i\vec{q}N_1\vec{a}_1} = e^{i\vec{q}N_2\vec{a}_2} = \ldots = 1 \tag{2.18}$$

Hence, by considering the boundary conditions to have Born-Von Karmen constraints[19] (equation 2.18), leading to the consideration of periodicity of wavevectors. The Fourier transform is then given by:

$$f\left(\vec{q}\right) = \frac{1}{\Omega_{crystal}} \int_{\Omega_{crystal}} d\vec{r} f\left(\vec{r}\right) e^{i\vec{q}\cdot\vec{r}} \tag{2.19}$$

$$= \frac{1}{N_{ce11}} \sum_{n_1, n_2 \ldots} e^{i\vec{q}\vec{T}(n_1, n_2 \ldots)} \frac{1}{\Omega_{cell}} \int_{\Omega_{cell}} d\vec{r} f\left(\vec{r}\right) e^{i\vec{q}\vec{r}} \tag{2.20}$$

From the last expression we can observe that the sum over lattice points is obtained by the non-zero outcome of the dot product $\vec{q} \cdot \vec{T}(\vec{n})$, and because the translation had the real space lattice vectors as basis we can obserbe that $\vec{q} \cdot \vec{a}_i = 2\pi n$ where $n \in \mathbb{Z}$. The reciprocal lattice vector with non-zero $f(\vec{r})$ Fourier transform is for $\vec{q} = \vec{G}$. This vector can be written as follows:

$$\vec{G}\left(m_1, m_2 \ldots\right) = m_1 \vec{b}_1 + m_2 \vec{b}_2 + \ldots \qquad , \qquad m_i \in \mathbb{Z} \tag{2.21}$$

Also, the Fourier transform for each vector $\vec{G}$ will be given in terms of the cell volume:

$$f\left(\vec{q}\right) = \frac{1}{\Omega_{cell}} \int_{\Omega_{cell}} d\vec{r} f\left(\vec{r}\right) e^{i\vec{G}\cdot\vec{r}} \tag{2.22}$$

2.2.2.1 Bloch's theorem

Due to the fact that the lattice is composed of atomic nuclei spaning the same Coulombic potential, with periodicity related to the lattice vectors, this potential may be expanded in Fourier space like this:

$$V(\vec{r}) = \sum_{G} V_G e^{i\vec{K}\cdot\vec{r}} \quad , \quad V_G = \frac{1}{\Omega_{ce11}} V(\vec{r}) e^{-i\vec{K}\cdot\vec{r}} dr \tag{2.23}$$

This periodicity, togheter with the Born-von Karman conditions depicted on equation 2.18 implies periodic behavior under this $\vec{q}$ wavevector. Therefore, the wavefunctions may be expressed like this:

$$\psi(r) = \sum_{q} c_q e^{i\vec{q}\cdot\vec{r}} \tag{2.24}$$

Taking this considerations into account, the Schrödinger equation (eqn. 2.4) can be written in reciprocal space as follows:

$$\left(-\frac{\hbar}{2m}\nabla^2 + \sum_{\vec{G}} V_{\vec{G}} e^{i\vec{G}\cdot\vec{r}} - E\right) \sum_{\vec{q}} c_{\vec{q}} e^{i\vec{q}\cdot\vec{r}} = 0 \tag{2.25}$$

$$\sum_{\vec{q}} \left(\frac{h^2 q^2}{2m} - E\right) c_{\vec{q}} e^{i\vec{q}\cdot\vec{r}} + \sum_{\vec{G},\vec{q}} V_{\vec{G}} c_{\vec{q}} e^{i(\vec{G}+\vec{q})\cdot\vec{r}} = 0 \tag{2.26}$$

$$\sum_{\vec{q}} \left(\frac{h^2 q^2}{2m} - E\right) c_{\vec{q}} e^{i\vec{q}\cdot\vec{r}} + \sum_{\vec{G},\vec{q}-\vec{G}} V_{\vec{G}} c_{\vec{q}-\vec{G}} e^{i(\vec{G}+\vec{q}-\vec{G})\cdot\vec{r}} = 0 \tag{2.27}$$

$$\rightarrow \sum_{\vec{q}} e^{i\vec{q}\cdot\vec{r}} \left[\sum_{\vec{q}} \left(\frac{h^2 q^2}{2m} - E\right) c_{\vec{q}} + \sum_{\vec{G}} V_{\vec{G}} c_{\vec{q}-\vec{G}}\right] = 0 \tag{2.28}$$

This final expression is represented in the next line, where all the coefficients in the sum involving the reciprocal vectors $\vec{q}$ must vanish, and after a change in indices we get:

$$\left(\frac{h}{2m}(\vec{k} - \vec{G})^2 - E\right) C_{\vec{k}\cdot\vec{G}} + \sum_{\vec{G}'} V_{\vec{G}'-\vec{G}} C_{\vec{G}-\vec{G}'} = 0 \tag{2.29}$$

The interpretation of this expression is that for any wavevector $\vec{k}$, only the ones that differ from it by $\vec{G}$ will hold the last vanishing condition with respect to the periodic potential expansion. Therefore, our wavefunctions, as long as the potential exhibits periodic behavior, can be written as:

$$\psi_k(\vec{r}) = \sum_{\vec{G}} e^{i\vec{k}-\vec{G})\cdot\vec{r}} = e^{i\vec{k}\cdot\vec{r}} \sum_{\vec{G}} c_{\vec{k}-\vec{G}} e^{i\vec{G}\cdot\vec{r}} \tag{2.30}$$

$$\psi_k(\vec{r}) = e^{i\vec{k}\cdot\vec{r}} u_{n,k}(\vec{r}) \quad , \quad \psi_{n,\vec{k}} = \psi_{n,(\vec{k}+\vec{K})} \tag{2.31}$$

The wavefunction in this representation is also known as *Bloch Wave*, and despite they do not explicitly give an analytical solution to $\psi(\vec{r})$, it tell us that for this kind of systems, the solutions can be represented by plane waves with amplitude $u_{n,k}(\vec{r})$ deppending on the shape of the potential. For any given value of k there is an infinite ammount of solutions for the periodic function $u_{n,k}$ representing the lattice. Hence, the quantum number n is also required to fully describe the state of the Bloch Wave.

2.2.2.2 Plane wave expansion

From the reciprocal space form of Schrödigner (eqn. 2.29), we can observe that by solving it, the solution will deppend on the wavevector $\vec{k}$, then we can solve it for each value of $\vec{k}$ independently. The solution, that can be expressed as a Bloch Wave (as 2.31) has the property of having periodic amplitude(eqn. 2.32)[13].

$$u_k(\vec{r} + n_1\vec{a}_1 + n_2\vec{a}_2 + \ldots) = U_k(\vec{r}) \tag{2.32}$$

This periodicity implies that this function can be expanded as an infinite sum of plane waves deppending on all possible values of $\vec{G}$ vectors satisfiying $\vec{G} \cdot \vec{a} = 2\pi n$, with $n \in \mathbb{Z}$ and $\vec{a}$ being a real space vector. The expansion is depicted in the next equation:

$$u_k(\vec{r}) = \sum_{\vec{G}} c_{\vec{G}} e^{i\vec{G}\cdot\vec{r}} \tag{2.33}$$

Now, combining equation 2.31 and 2.34 leads to the next definition. We can observe the expression to tell us that for any specific solution of $\vec{k}$, we have to solve this infinite summation involving all the possible values of $\vec{G}$.

$$\rightarrow \psi_k(\vec{r}) = \sum_{G} c_{\vec{k}+\vec{G}} e^{i(\vec{k}+\vec{G})\cdot\vec{r}} \tag{2.34}$$

In order to make it computationally achievable, the sum has to be truncated. We can note, that the kinetic energy (2.35) of this solutions will be proportional to the wavevector of each plane wave in the summation. Therefore, since we are interested on ground state properties in our system, the lower kinetic energies will give us more physically relevant information than higher ones.

$$E_{kin} = \frac{\hbar^2}{2m}|\vec{k} + \vec{G}|^2 \tag{2.35}$$

2.2.3 Pseudopotentials

By using pseudopotentials, one might greatly reduce the computation of individual electrons of the inner shells. The method is commonly used also in atomic physics and neutron scattering problems. The pseudopotential construction consists of replacing the highly complicated expressions of the Coulombic interactions by a simplier effective potential containing the overall charge interaction effects of the inner electron shells plus the atomic nucleus[22].

For calculating scattering amplitudes from an spherically symmetric potential, the phase shift of the sctattered wave is required to get information about the cross-section and other properties of the wavefunction far from the scattering region[15]. Hence, the phase shift becomes a very important quantity to understand the behavior under scattering events. The potential strength is directly proportional to the phase shift the wave gets. By constructing a proper pseudopotential, a more accurate description of the scattering event is obtained under a wider energy range[19].

The usage of pseudopotentials in solid state physics applications started with the work of Hellman, who constructed effective potentials to study scattering events of the valence electrons with the ionic components in a metallic lattice[23]. He developed this construction while formulating a theory of binding for metallic materials[24]. Few years later, there was found that equations describing behavior of valence electrons can be achieved via weak effective potentials, and a great set of sp-bonded metals and semiconductors was acurately described using a few empirical coefficients[25]. More accurate and reliable pseudopotential methods were developed since then, first by getting a wider range of materials reliably described for specific problems like crystal phase stabilities[26]. Later on, more problems were getting solved, such as conserving the norm of the obtained wavefunctions[27], improving the 'softness' (separating the resulting wavefunction into an overall smooth part plus a rapidly oscillating part around the ion cores) of the pseudopotentials[28], and reduced computational costs[29]. Nowadays, there is a plenty of pseudopotentials widely available to be used into the different DFT rountines inside the multiple simulation codes available.

2.2.4 The Projector Augmented Wave (PAW) method

Some 'soft' or 'ultrasoft' pseudopotentials still have a disadvantadge at the moment of restoring the true valence wavefunction. This reason motivated the work of Blöchl[30] to construct a method for accurately partitioning the electron wavefunctions to avoid this problems. He proposed to calculate the all-electron wavefunction for every electron, not only the valence ones as in the usual pseudopotential method in order to have access to the complete wavefunction. Later, combines the computational advantadge of the Vanderbilt[31] ultrasoft pseudopotentials in such a way that not so many plane waves are needed to fill up the expansion describing the wavefunction of the valence electrons.

The electronic wavefunctions are split into three terms:

$$\varphi = \tilde{\varphi}_v + \chi_v - \tilde{\chi}_v \tag{2.36}$$

The first term $\tilde{\varphi}$ perfectly matches the wavefunction outside the atomic core region. The second function χ_v is exact inside this mentioned region (highly oscillatory near the core) and slowly decays to zero outside of it, and finally $\tilde{\chi}_v$ is equal to the smooth and highly localized parts of the $\tilde{\varphi}$ and matched the χ_v part outside the core regions. Therefore, this last term cancels out all the non-physical waves used in the method. This procedure allows us to calculate the total electronic energy by parts, and thus letting us have all-electron solutions easily[32]. A complete routine for this method is implemented on VASP.

2.3 Principles of Density Functional Theory

By applying the later mentioned approximations, we can get rid from the ion-ion interactions and the nuclei kinetic energies. Then, equation 2.37 becomes simpler:

$$\left[-\sum_i \frac{\hbar^2}{2m_e}\nabla_i^2 + \frac{1}{2}\sum_{i\neq j}\frac{e^2}{4\pi\varepsilon_0}\frac{1}{\left|r_i - r_j\right|} - \frac{1}{2}\sum_{i,I}\frac{e^2}{4\pi\varepsilon_0}\frac{Z_i}{\left|r_i - R_I\right|}\right]\psi(\mathbf{r}, t) = E_{total}\psi(\mathbf{r}, t) \tag{2.37}$$

The many-body problem is then considered as a one-body problem by stablishing an electron density cloud, composed of the electrons moving along the material. The cloud is given by the probability of finding a particle at a position **r**:

$$\rho(\vec{r}) = \langle\psi(\mathbf{r})|\psi(\mathbf{r})\rangle \tag{2.38}$$

Now, assuming that the expected value of the *total energy* obtained from the Hamiltonian is only dependent on the electron density, we may write:

$$\begin{aligned} E_{\text{Total}}[\rho] &= \langle\psi|\, T + V_{\text{e-e}} + V_{\text{ext}}\, |\psi\rangle \\ &= F[\rho] + \langle\psi|\, V_{\text{ext}}\, |\psi\rangle \\ &= F[\rho] + \int \rho V_{\text{ext}}\, d^3\vec{r} \end{aligned} \tag{2.39}$$

where we define a universal functional $F[\rho]$ that contains all the electron interaction and energies: kinetic, Coulombic, and *exchange − correlation* energies, and can be written as:

$$F[\rho] = T[\rho] + V_{\text{e-e}}[\rho] \tag{2.40}$$

$$= T[\rho] + V_C[\rho] + E_{\text{xc}}[\rho] \tag{2.41}$$

$$= -\frac{\hbar^2}{2m_e}\langle\psi|\,\nabla^2\,|\psi\rangle + \frac{1}{2}\int\int\frac{\rho(\vec{r})\rho(\vec{r}')}{|\vec{r} - \vec{r}'|} + E_{\text{xc}}[\rho] \tag{2.42}$$

This shows that the nature of the new energies depends on the applied universal functional.

2.3.1 The Hohenberg-Kohn theorem

The assumption stipulated before that stated the total energy of a many-body electronic system can be expressed as a functional of the electron density (eq. 2.38) is known as Hohenbeg-Kohn theorem. This theorem is based on the following considerations: First, the ground state of the electronic density ρ_{gs} is uniquely given by the potential generated by the nuclei in the lattice V_{n-e}; second, there is a one-to-one correspondence to the expression of the external potential applied V_{n-e} and the many-body electronic wavefunction Ψ involved; and lastly, the total energy

E is uniquely described by a state describing the latter wavefunction Ψ. Therefore, by following the sequential logic of these arguments

$$\rho \rightarrow V_{n-e} \rightarrow \Psi \rightarrow E \tag{2.43}$$

we can infer that the total energy must be a functional of the density: $E = F[\rho]$. This theorem may be easily proven by *reductio ab absurdum* considering the existence of two different external potentials: V_{ext} and $V_{ext}^{'}$. The procedure goes as follows:

Two different Schrödinger equations can be stated, where distinct energies will result from the different potentials.

$$(T + V_{ext}^{'} + V)\psi_0 = E'\psi_0 \qquad\qquad (T + V_{ext} + V)\psi_0 = E\psi_0 \tag{2.44}$$

As they are acting over the same ground state ψ_0, summing both equations leads to:

$$(V_{ext}^{'} - V_{ext})\psi_0 = (E' - E)\psi_0 \tag{2.45}$$

Leading to a contradiction because for this equation to hold the potentials have to be equal $V_{ext} = V_{ext}$, but from the initial assumption this cannot be. Therefore, the ground state density is unique given an specific external potential.

2.3.2 Kohn-Sham equations

The *Hohenberg – Kohn* theorem[33] ensures the existence of a universal functional, but does not tell us anything about how to construct it. Also, it states that the external potential (lattice of the solid) is unique for a given ground-state electron density.

The full Hamiltonian of the interaction (eq. 2.37) strictly depends on the charge density alone; thus, it now becomes:

$$\sum_{i=1}^{N}\left[-\frac{\hbar^2}{2m_e}\nabla_i^2 + \left.\frac{e^2\rho(\vec{r_i})}{|\vec{r_i} - \vec{r_j}|}\right|_{j\neq i}\right] - \sum_{\alpha=1}^{N}\frac{Z_\alpha\rho(\vec{r_i})}{|\vec{r_i} - \vec{R_\alpha}|} + V_{xc}(\vec{r_i})\Bigg] = \epsilon_i\psi(\vec{r_i}) \tag{2.46}$$

Now, the most important property of an electronic ground state density is its energy, which may be calculated by variational calculus[34]:

$$E_{\mathrm{gs}} = \min_{\psi}\langle\psi|\,\hat{H}\,|\psi\rangle \tag{2.47}$$

Also, we can minimize the universal functional in equation (2.40) such that the obtained wave function is consistent with a charge density ρ, as follows:

$$\begin{aligned} F[\rho] &= \min_{\psi\rightarrow\rho}\langle\psi|\,T + V_{\mathrm{e-e}}\,|\psi\rangle \\ &= \left\langle\psi_{min}^{\rho}\right|T + V_{\mathrm{e-e}}\left|\psi_{min}^{\rho}\right\rangle \end{aligned} \tag{2.48}$$

Since the ground state of the system will be the configuration with minimal energy, considering the equation (2.39), we have the following relation:

$$\begin{aligned} E_{\mathrm{Total}}[\rho] &\geq E_{\mathrm{gs}}[\rho] \\ \langle\psi|\,V_{\mathrm{ext}}\,|\psi\rangle + F[\rho] &\geq E_{\mathrm{gs}} \end{aligned} \tag{2.49}$$

In general, the expectation value of V_{ext} will not change by choosing either basis ψ or ψ_{gs}. Therefore:

$$\left\langle \psi^{\rho}_{min} \right| T + V_{\text{e-e}} \left| \psi^{\rho}_{min} \right\rangle \geq \left\langle \psi_{gs} \right| T + V_{\text{e-e}} \left| \psi_{gs} \right\rangle \tag{2.50}$$

but after the minimization, the obtained energy of the system will correspond to the ground state. Then, the latter expression is only true for:

$$\left\langle \psi^{\rho}_{min} \right| T + V_{\text{e-e}} \left| \psi^{\rho}_{min} \right\rangle = \left\langle \psi_{gs} \right| T + V_{\text{e-e}} \left| \psi_{gs} \right\rangle \tag{2.51}$$

Therefore, this ensures us that, after iterations, we converge to the ground-state energy:

$$\begin{aligned} E_{\text{gs}} &= \int \rho_{\text{gs}}(\vec{r}) V_{\text{ext}}(\vec{r})\, d^3\vec{r} + \left\langle \psi_{gs} \right| T + V_{\text{e-e}} \left| \psi_{gs} \right\rangle \\ &= \left\langle \psi_{\text{gs}} \right| V_{\text{ext}} \left| \psi_{gs} \right\rangle + F[\rho_{gs}]. \end{aligned} \tag{2.52}$$

To obtain the correct energies, we have to use calculus of variations to minimize the charge density. We will denote a small Functional Variation with δ. Therefore, we will look for extreme values of the charge density:

$$\int \delta\rho(\vec{r}) d^3\vec{r} = 0 \tag{2.53}$$

Hence, considering the total energy expression in equation 2.39, we want to minimize it to approach the ground-state energies:

$$\begin{aligned} E_{\text{Total}} &= V_{\text{n-e}}[\rho] + V_{\text{e-e}}[\rho] \\ &\quad + T[\rho] + E_{\text{xc}}[\rho] \geq E_{\text{gs}}[\rho] \\ &= \int \rho_{\text{gs}}(\vec{r}) V_{\text{n-e}}(\vec{r})\, d^3\vec{r} \\ &\quad + \int\int \frac{\rho(\vec{r})\rho(\vec{r}')}{|\vec{r}-\vec{r}'|} d^3\vec{r} d^3\vec{r}' \\ &\quad + T[\rho] + E_{\text{xc}}[\rho] \end{aligned} \tag{2.54}$$

Applying variations to the energy functional:

$$\begin{aligned} \delta E_{\text{Total}} = \int \delta\rho \Bigg[& V_{\text{n-e}} + \int \frac{\rho(\vec{r}')}{|\vec{r}-\vec{r}'|} d^3\vec{r}' \\ & + \frac{T[\rho]}{\delta\rho}\bigg|_{\rho=\rho_{\text{gs}}} + \frac{E_{\text{xc}}[\rho]}{\delta\rho}\bigg|_{\rho=\rho_{\text{gs}}} \Bigg] d^3\vec{r} = 0 \end{aligned} \tag{2.55}$$

In order to wrap up some terms, we can define an external potential and an extra effective potential associated with the exchange-correlation energy:

$$V_{\text{xc}}(\vec{r}) = \frac{E_{\text{xc}}[\rho]}{\delta\rho}\bigg|_{\rho=\rho_{\text{gs}}} \tag{2.56}$$

$$V_{\text{eff}}(\vec{r}) = V_{\text{n-e}} + \frac{E_{\text{xc}}[\rho]}{\delta\rho}\bigg|_{\rho=\rho_{\text{gs}}} + \int \frac{\rho_{\text{gs}}(\vec{r}')}{|\vec{r}-\vec{r}'|} d^3\vec{r}' + V_{\text{xc}}(\vec{r}) \tag{2.57}$$

Thus, equation (2.55) becomes:

$$\delta E_{\text{Total}} = \int \delta\rho \left[\frac{T[\rho]}{\delta\rho}\bigg|_{\rho=\rho_{\text{gs}}} + V_{\text{eff}}(\vec{r}) - \varepsilon \right] d^3\vec{r} = 0 \tag{2.58}$$

where ε represents a Lagrange multiplier that contains the constraint of particle conservation for the minimization process[35]. Finally, the whole problem can be reduced to solve the following one-particle equation that contains all the many-body interactions wrapped up into an effective potential, as previously defined. This is the Kohn-Sham equation:

$$\left(-\frac{\hbar^2}{2m}\nabla^2 + V_{\text{eff}} - E_j \right) \phi_j(\vec{r}) = 0 \tag{2.59}$$

$$\rho_{\text{gs}}(r) = \sum_{j=1}^{N} |\phi_j(\vec{r})|^2 \tag{2.60}$$

This set of equations is self-consistent[36] and can be iterated over and over again starting from a homogeneous electron gas or an inhomogeneous one[33], depending on the *ansatz* applied over the system. After the first set of solutions and eigenenergies are obtained, a new electron density is calculated from the previously calculated wave functions until energy convergence is achieved.

To accelerate the calculations, the wave functions are expanded under a Fourier series, depending on the boundary conditions of the problem (a periodic lattice would allow us to consider Bloch waves[37]) and are cut off up to an arbitrary energy value so that convergence is unaffected[13].) Also, extra symmetry points are obtained within the first Brillouin Zone to reduce the wave function calculation complexity[38].

2.3.3 The Exchange and Correlation Functionals

The second Hohenberg-Kohn theorem ensures the existance of a functional that accurately describes the ground state electronic density of a given system[33], but it does not give us directives about its form and how to construct it.

2.3.3.1 The Local Density Approximation (LDA)

Multiple approaches to get the exchange-correlation energy exist nowadays, one of the simplest ones involve obtaining energies from an homogeneous electron gas of relative high density (same as considering the kinetic energy of the gas to be higher than the potential energy acting over it). The functional form of LDA goes as follows:

$$E_{xc}^{LDA} = \int \rho_{gs}\left(\vec{r}\right) E_{xc}\left[\rho_{gs}\left(\vec{r}\right)\right] d\vec{r} \tag{2.61}$$

The LDA functional becomes exact just for the case of an homogeneous electron gas, for example: electrons standing in vacuum affected by an homogeneous potential to neutralize the overall charge over space. The energies are easily calculated due to the fact the Kohn-Sham eigenfunctions come out simply from Slater determinants of the plane waves involved[39].This method is not very accurate since most of the analyzed systems present inhomogeneities in tis electronic gas clouds. Therefore, gradient corrections may be performed (see next subsection). In general, for getting the total energy quantum Monte-Carlo methods are used to determine the random cloud interactions that contribute to the correlation energies $E_c[\rho(\vec{r})]$.

In this context, the expression for the total energy can be given as:

$$E_T = V_{n-e} + V_H + V_{e-e} + T + \int d^3\vec{r}\rho \left\{E_x\left[\rho(\vec{r})\right] + E_c\right\} \tag{2.62}$$

Where V_H is the Hartee energy asociated to the energies obtained from solving the Schrödinger equation by considering weak electron-electron interactions, and therefore solutions in the form of one-electron wavefunctions to compose an Slater determinant for describing the many-body wavefunction[40]. Although the LDA functional has this poor assumptions it has been demonstrated remarkable results through multiple calculations. The main reason for that is the achievement of holes obeying the summation rules for particular hamiltonians[41]. Therefore, even though arbitrary approximations are imposed, holes still satisfy the contraints of the sum rules. Besides, since its exchange-correlation energy contains only the spherical average of holes, their detailed shape have no effect to the overall result. Another important thing to consider about LDA is the fact that it is known to underestimate the value of the band gap of materials[42].

2.3.3.2 The Generalized Gradient Approximation(GGA)

The first thing to improve from the LDA functional is the deppendance on a perfectly homogeneous gas to be exact. Hence, in the GGA functional, the gradient of the electronic density is considered. At the early beginnings of the construction of this LDA 'improvements', the proposed "Gradient Expansion Approximation" methods did not make a great improvement over the LDA functional. Despite of this time considering the gradient in the fucntional expression and getting known values for its first order expansions, the sum rules became violated along other constraints[43]. Mainly due to the problem that charge densities in some real materials are very inhomogeneous, leading to very high gradient magnitudes. Those magnitudes cause the expansions blow up and return worse results, even than LDA.

Later on, the GGA was proposed to modify this large gradients in such a way this large magnitudes are not a problem anymore. The expression for the GGA functional is expressed as:

$$E_{xc}^{GGA}\left[\rho\left(\vec{r}\right)\right] = E_{xc}^{LDA} + \alpha\left|\frac{\nabla\rho\left(\vec{r}\right)}{\rho^{4/3}}\right| \tag{2.63}$$

The extra factor that scales the exchange-correlation energy of the LDA functional is also called enchancement factor $F_x(s)$.

$$F_x\left(s\right) = 1 + s = 1 + \left(\frac{1}{2(3\pi^2)^{1/3}}\right)\frac{|\nabla\rho|}{\rho^{4/3}} \tag{2.64}$$

2.3.3.3 The optb86-vdW functional

The motivation of studying biomolecules, such as DNA, where electronic dispersion effects become important pushed theoretical DFT research towards the development of a functional capable of taking into account the non-local interactions present in such systems. At first, van der Waals effects were succesfully implemented and got qualitative good results just for layered structures[44]. Later on, further research lead to the development of a more sophisticated functional deppending on a kernel with parameters relying on the local and gradient density. This functionals were able to correct the exchange-correlation energies regardless of the geometry of the studied material[45].

The achieved results from the generalized geometry van der Waals functional were not reliable enough as they did not fullfil chemical accuracy for important biomolecules (set S22 of dimers). Thus, different exchange functionals were re-tuned in order to optimize the binding energies of those molecules[46], giving birth to the optb86-vdW functional[47].

The form of the expression for the energy in vdW-DF is given by:

$$E_{xc} = E_x^{GGA} + E_c^{LDA} + E_c^{nl} \tag{2.65}$$

The GGA exchange part is computed from the revPBE density functional, the LDA part again from Monte-Carlo methods, and a non-local term E_c^{nl} containing all the correlation interaction effects. The non-local term is computed by using a double space integration from a response function model describing the random electronic densities interactions[48], allowing an improvement over the former methods. This non-locality is[49] found to become more important with transition metals with complete *d* shell, as such effects become significant against the GGA exchange energies. Further parameter optimization lead to the development of the optb86-vdW functional[49]. It has shown improved results for metals, ionic compounds and metals, hence opening the path towards new research and more accurate values for lattice constants, bulk moduli and atomization energies.

2.4 Electron Microscopy

In the seventeenth century, thanks to the simultaneous parallel work of Robert Hooke and Antoni von Leeuwenoek, humanity discovered the existence of microbes (or *animalcules* as von Leeuwenhoek himself coined them)[50]. Despite of the low magnifying power of their first prototypes of about 25-fold to 200-fold, they were able to report the first images of protozoa, bacteria and microfungus. Since then, the development of more powerful microscopic techniques has become a cornerstone to scientific research, allowing us to probe the world at small scales. Later, in the decade of 1929, the nuclear physicist Leo Szilard would propose the construction of a microscope that may use electrons instead of light beams to probe samples in order to improve the currently available resolution. It is until 1931 when Ernest Ruska, together with Max Knoll, build the first transmission electron microscope (TEM) with a magnifying power of 17.3-fold. Ruska and Knoll, were conscious about the fact that optical microscopy has a limit because of the wavelength of light used[51]; they simply hoped for electrons to have a low dimensions compared with light waves. As engineers, they were not aware of the current developments of de Broglie matter waves, even most physicists at that time were not neither. Later, after Ruska got to know about the de Broglie equation, he became motivated again to continue using electrons as they display a de Broglie wavelength about five orders of magnitude shorter than light waves. Two years later, Ruska successfully improved his design being able to first surpass the optical microscope attainable resolution. After the end of the Second World War, the production of electron microscopes became very profitable for the industry and its use also widely increased in the scientific research. In the year of 1986, Ruska was awarded with the Nobel Prize in physics for its prototype schematics, together with Gerd Binnig and Heinrich Rohrer for the development of Scanning Tunneling Microscopy (STM)[52].

2.4.1 Scanning Tunneling Microscopy

During the early 1980s, at IBM Laboratories in Zurich, Switzerland, G. Binning and H. Rohrer developed the principles behind nowadays STM technology. While trying to measure the distribution of tunneling current between a superconducting surface and a metallic tip with a separation distance of about 1 nm, for analyzing semiconducting properties, they realized the tremendous potential resolution attainable with this technique. Their achievement of getting atomic resolution by using the tunneling effect over samples with electrical conductivity opened the path of STM development and its consequences triggered the advancement of fields like nanotechnology. This technique lead to the possibility of probing the electronic density of states of materials with respect to the measured tunneling current I by changing the voltage V applied over the tip and the sample. Of course, the spatial resolution also depends on the sharpness of the tip apex. In an ideal case, having a one-atom tip within an stable tip basis is required. Since the electron wavefunctions of the tip depend on the atomic species used on it it is fundamental to keep control over this, otherwise it may affect the overall measurements[53].

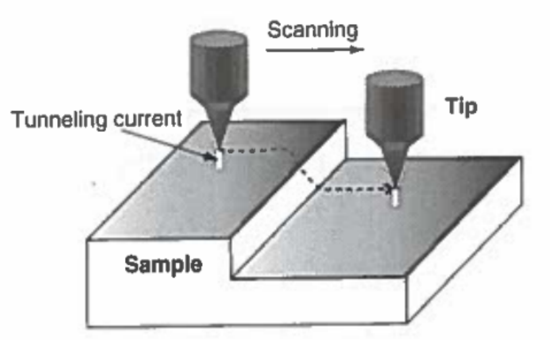

Figure 2.1: Diagram describing the basic working principle of an STM device. Adapted from Ref. 53

2.4.1.1 Line-scan STM mode

The STM device measures the absolute value of the current passing through the tip-sample interface. Also, due to the exponential decrease of the tunneling effect by increasing the distance, it is possible to measure slight changes in separation between the top-most atomic orbitals and the tip by just measuring the tunneling current. Therefore, by laterally scanning the surface of the sample, adjusting the tip height in such a way the tunneling current keeps constant, one can probe the topography of the sample. By considering a one-dimensional barrier composed of a vacuum-metal interface we can give an approximate form to the tunneling current present in a typical STM construction, also assuming a constant density of states at the tip is constant with respect to the electron energies and elastic interactions we can write the tunneling probability, I[54]:

$$I \approx \frac{4\pi e}{\hbar} |M|^2 \rho_t(0) \int_{-eV}^{0} \rho_s(\varepsilon)\, d\varepsilon \tag{2.66}$$

Where the $\rho_s(\varepsilon)$ function represents the Local Density of States at energy ε. By considering the fact that it is not possible to probe and get absoulte heights of the topographies of the sample because it changes given the applied V_{BIAS}, a naïve approach would be to chose a contour of current charge density. Nevertheless, equation 2.67 suggests that this current is given by the charge density below the Fermi level, where V is the applied bias voltage.

This current intensity Slightly changing the separation of the tip from the specimen, for example from 1 nm to 0.1 nm one can achieve total change in tunneling current of about one order of magnitude. Therefore, atomic resolution can be accomplished in the z direction, and also a lateral resolution up to 0.2 nm is achievable. The resulting spatial profile is a topological image of the sample, see Fig. 2.2.

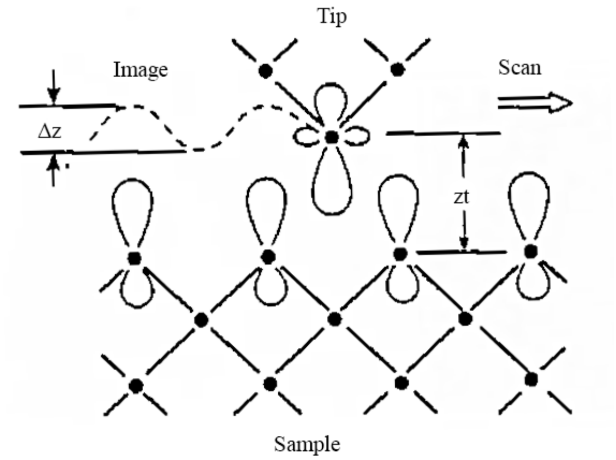

Figure 2.2: Microscopic view of the tip interaction with the protruding orbitals of the surface of the sample. Adapted from Ref. 54

2.4.1.2 Density of States

From solid state physics theory[55], the Density of States (DoS) represents the number of electronic states contained within an energy range, where a high DoS value for an specific energy level means that many states are availiable for electrons to occupy.

Equation 2.67 suggests that by keeping a constant tip-sample distance at an specific point in a xy-plane perpendicular to the probe, and setting a negative bias voltage, the current becomes exact the following expression:

$$I = I_0 \int_{-eV}^{0} \rho_s(\varepsilon)\, d\varepsilon \tag{2.67}$$

Therefore, by stablishing such conditions and varying the bias voltage V on the probe it is possible to measure the integral of the density of states around $-eV$ energy units below the Fermi level. And deppending on the sign of the applied voltage, positive or negative, one can measure the tunnelling electrons of the unoccupied states (tip to sample electrons) and occupied (from sample to tip) ones respectively.

2.5 Simulation Software

In this section, the software used and its main characteristics are detailed and discussed. Among the most popular codes available for performing DFT are GAUSSIAN and VASP. GAUSSIAN is one of the most oldest and widely used DFT codes, with its theoretical background being born with the work of John Pople[56].

Therefore, the most important code used in the development of this thesis was VASP, which contains the plane wave DFT algorithms needed to perform our calculations. Then, some additional resources are used in parallel, such as visualization tools and atomic manipulation applications to handle the input and output files coming out from the VASP code or performing other extra calculations over our structures.

2.5.1 VASP: Vienna Ab initio Simulation Package

After the great discovery of a self-consistent procedure to calculate the ground state properties of many-body systems by Walter Kohn[36], early DFT codes started being developed by considering different procedures to make it computationally feasible[57]. The first DFT code development was lead by John Pople, in which he proposed the usage of a Gaussian-like basis sets to compute molecular orbitals[58]. This procedures became available in the GAUSSIAN code, very popular among theoretical chemists to calculate properties for complex molecules. But, a solid-state code for materials science was needed, and VASP became a reliable code. The VASP package applies psudpotentials to carry on plane-wave calculations over periodic solid systems. As in all DFT codes, the Kohn-Sham equations are solved in a self consistent manner expanding the orbitals as a combination of functions coming out from an specific chosen basis set. The VASP code implements plane waves (PW) basis set, which in practice offers the following two advantages[59]:

- Good control of the convergence coming out from the chosen basis set: Usually, the PW method offers good convergence and accuracy versus other basis sets. Very large basis sets (something that is computationally expensive) have to be used in order to match up PW calculations[60]. The phrase "PW accuracy" is now popular among nowadays DFT scientists
- The process of evaluation of forces and stress acting on our system can be easily calculated by applying the Hellmann-Feynman theorem[61]. Something that allows further molecular dynamics calculations.

Additionally, since the properties of materials depends mainly on the valence electrons, VASP simplify the problem by replacing the core electrons by the projector augmented wave method (PAW)[30], the results are comparable to an all-electron code calculations.

Many other sophisticated (but computationally expensive to perform) exchange correlation functionals are availiable inside the VASP code. Such as post-DFT corrections like RPA, GW many-body perturbation theory and many other hybrid functionals to further correct the total energies involved in the case of study.

Given the fact that just solving the Kohn-Sham equations do not complete the set of tools needed for top-level materials research, VASP has multiple routines to further calculate properties of solid-state structures such as: vibrational modes spectra computation, mechanical properties prediction, phase transformation activation energies, magnetic properties and so on. In conclusion, VASP constitutes a reliable tool, with a good mixture of genetic algorithms for studying crystalline and surface structures[62].

2.5.2 ASE: Atomic Simulation Environment

An object-oriented open-source python code with multiple tools for visualization, set up, and analysis of atomistic calculations, regardless of the DFT code used to get the data. It was initially designed because of the big need of a tool allowing an intuitive approach to manipulate the input and output files of the multiple available DFT codes[63]. In early 1990s, almost all the computational physics applications were coded in FORTRAN or C, and a good background programming skill were required to handle those applications, and even more to modify them. Those were the pioneering times for Object-Oriented Programming (OOP), and, despite of its multiple advantages, it was not very popular among computational physicists. The potential use of OOP into physics coding would lead to a more intuitive way to manipulate parameters and analyze data coming out from calculations, without the need of having to do unnecessary coding. So, there were proposals trying to make programming inside the field of computational physics more easy to implement. For example, Dubois presented a programmable architecture with a run-time database manager with a set of commonly used data structures and functions for the user to just invoke them directly without constructing them from scratch. Also, he added an interpreter software for parsing input, letting the user to execute commands easily[64]. By considering multiple of this proposals to improve scientific coding in the DFT community, the first version of ASE was born[65] by implementing OOP into the input/output data from DFT codes. Therefore, by using of python classes one can easily grasp that such a class would store variables and methods specific to their class type. For example, the class "Atoms" can have "get positions" as a method to extract the coordinates in a python list; or objects like "Calculator" may contain properties related to the DFT parameters of the simulation code. Then, ASE works as a great front-end to perform tasks regardless of the DFT code. The most used feature in the development of this thesis was the Graphical User Interface (GUI) to read the atomistic positions of the input/output files from VASP.

2.6 The CaF_2/Si(100) interface

To clearly depict the interface of interest, we have to break it down into the details of each of its constituents. The silicon surface properties and how it is related to its bulk form is described, then the known properties of them. Later, a description of the CaF_2 compound is presented and the process in which the ultra-thin layers of it are grown into a pure Si(100) surface via the Chemical Vapor Deposition (CVD) method.

2.6.1 The Si(100) surface

Silicon, on its mineral forms, makes up to 90% of the Earth's compounds, and it is also found on relatively high abundances on other rocky planets of our solar system. On Earth, it is the second most abundant element (making up to 28% of its mass) of its crust after Oxygen[66].

Bulk silicon was first detailed by Lavoisier in 1787, where he described it as an oxide formed together with another chemical element[67]. Then, were Gay-Lussac and Thénard who first synthesized impure amorphous silicon by reacting silicon tetrafluoride over heated an isolated sample of metallic potassium[68], but they did not recognize it as a new element. Later, in 1823 Berzelius, using the same methodology as Gay-Lussac and Thénard, further purified the remaining brownish powder by washing it and identified the product as a new element, silicon[69].

Just recently, in the end and early 20th century the semiconductors industry began to rise, mainly based on germanium and galena crystals to build radio crystal detectors, Chandra Bose in 1901 would fill a U.S patent detailing his galena crystal rectifier[70]. Silicon radio crystals were not used as much as germanium ones because the latter demonstrated a higher carrier mobility, until Atalla in 1959 found a way of surface passivation by thermally oxidizing the silicon crystal forming SiO_2[71]. This lead to higher electrical conductivity because now the surface dangling bonds would not trap electrons, allowing the electron flux to easily reach the semiconducting bulk silicon inside the crystal[72].

Due to its paramount importance for the semiconductors industry, silicon surfaces analysis has been a increasingly active topic for materials science research. Specially, the interface SiO_2/Si(100) because of its importance for the construction of films for CMOS transistor technologies[72]. Over the last 20 years, the Si(100) surface has been deeply studied under experimental and theoretical frameworks[73]. The first microscope details of the atomic structure of this material was discovered by Schiler and Farnsworth[74] where they reported the existence of a 2×1 and proposed a periodic structure based on the formation of tilted silicon dimers. Later on, Wolkow[75] would be the first scientist to achieve a direct observation of the tilted silicon dimers on the Si(100) surface using a variable-temperature STM imaging in ultra high vacuum.

Experimentally, in order to construct a surface from the bulk silicon chemical etching procedures are applied to get wafers. Those products are then outgassed at Ultra High Vacuum (UHV) at 850 K for some hours and later flashing them at 1200 K for a few seconds[76]. After the cleavage of the bulk silicon across the (100) plane, some dangling bonds will remain in the top of the surface. The Si crystal structure has a face center cubic (fcc) lattice, then Si(100) surface is equivalent to the Si(001) direction.

Ideally, the fcc diamond-like structure of Si can be cleaved along the (100) Miller plane, leading to a 1×1 surface symmetry (see Fig. 2.3(a)). But, those dangling bonds are observed to reconstruct the surface geometry to achieve a lower energetic configuration. Hence, the dangling silicon bonds connect each other and lead to the observation of a 2×1 periodicity[77] (see Fig. 2.3(b)).

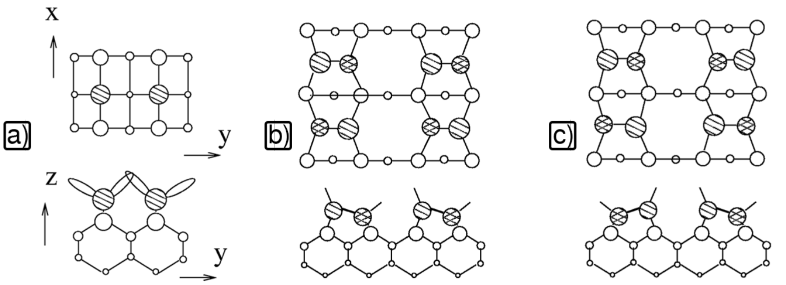

Figure 2.3: Geometries of the reconstruction of the surface after the cleavage through the (100) direction. a) clean cut immediately after the cleavage, b) $p(2 \times 2)$ buckled dimer configuration, c) $p(4 \times 2)$ buckled dimer configuration. Adapted from Ref. 78.

Moreover, not just parallel dimer formation with respect to the surface do form, but also asymmetric dimer (AD) formation are observed to occur. The dimerization of those silicon atoms lead to a reduction of the dangling bonds of the cleaved surface by half. The AD formation further decreases the surface free energy, therefore it represents the ground state configuration of the Si(100) (Fig. 2.3(c)). The asymmetry of the dimers is produced by a change of height of one silicon atom with respect to the other. Charge transfer occurs from the upper dimer to the lower one, filling the dangling bond of it at the expense of the former one[78]. Therefore, along the Si(100) surface parallel dimer rows get formed, but the orientation of the ADs is not uniform and they are not static.

The STM images taken at room temperature display just a time average of the switching between orientation of their asymmetries. The asymmetry of the silicon dimers on the surface is also known of *buckling*. Along the dimer rows of the surface, 'in-phase' orientation of the buckled dimers lead to a $p(2 \times 2)$ configuration (Fig. 2.3b) and 'out-of-phase' buckling constitute a $p(4 \times 2)$ geometry (Fig. 2.3c). Despite the $p(4 \times 2)$ is the most stable configuration, the difference in energies between those two buckling types is found to be less than 0.01 eV per dimer, then, historically, it went outside the computational accuracy to find the most stable configuration[11].

2.6.2 Electronic and structural properties of fcc Si and Si(100).

The experimental values describing the bulk structure of fcc silicon are already deeply studied and well known[79]. The remarkable property is its low energy band gap (1.11 eV at room temperature and 1.17 at 0 K[80]), allows it to be used for constructing semiconducting devices. It may be doped (electron donors/acceptors) using elements with different electronic configuration to get *n-doped* silicon or *p-type* silicon. The Fermi level and availability of charge carriers change as depicted in figure 2.4. Some of the bulk main properties are listed in Table 2.6.2.

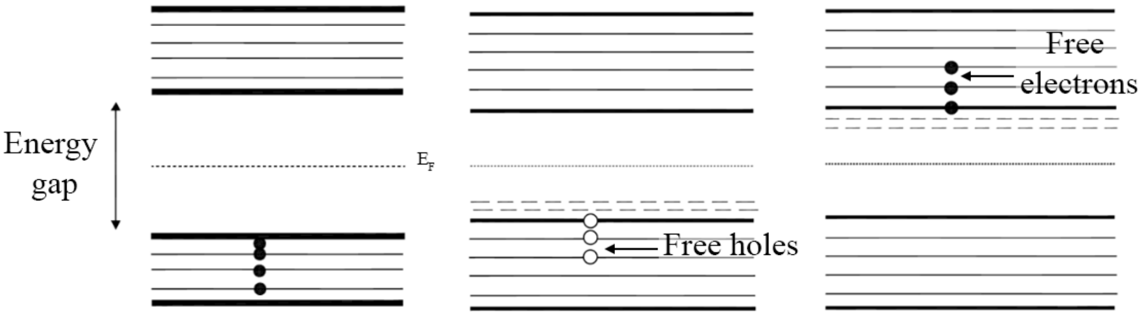

Figure 2.4: Band gap displayed by different silicon semiconductor types. a) pure silicon, b) n-doped silicon, c) p-doped silicon. Adapted from Ref. 79

Parameter	Physical value
Compatible acceptors	Al, B, Ga
Compatible donors	Sb, As, P
Atomic density	5.02×10^{22} atoms/cm^3
Bulk modulus	95-105 GPa
Crystal structure	Diamond cubic
Energy gap	1.12 eV
Space group	$Fd\overline{3}m$ Å
Silicon radius	1.18 Å
Lattice constant	5.429[81] Å

Table 2.1: Some values detailing the properties of bulk silicon at room temperature[79]

Considering the Si(100) surface, the electronic structure around the valence band maximum(VBM) is given by the spatial disposition of the dangling bonds, and hence important values such as the energy band gap strongly depend on the arrangement of those bonds. Given the fact that multiple doping, temperature and defect configurations vary from one experimental setup to another, a relatively large range of values have been reported in the literature for the Fermi energy, specially with respect to the occupied surface state belonging to the topmost silicon atom of the buckling dimers[82]. The minimum indirect band gap for the $c(4 \times 2)$ reported by STM experiments is 0.9 eV[83], and some GW quasiparticle calculations published by Northup[84] are also consistent with this value. This gap is mainly attributed to the bandwidth of the surface states of the buckling dimers: the $\pi_{1,2}$ and $\pi^*_{1,2}$ occupied and unoccupied states, respectively[11]. For the symmetric dimer configuration those π bonding and π^* antibonding states overlap, and thus the surface becomes metallic.

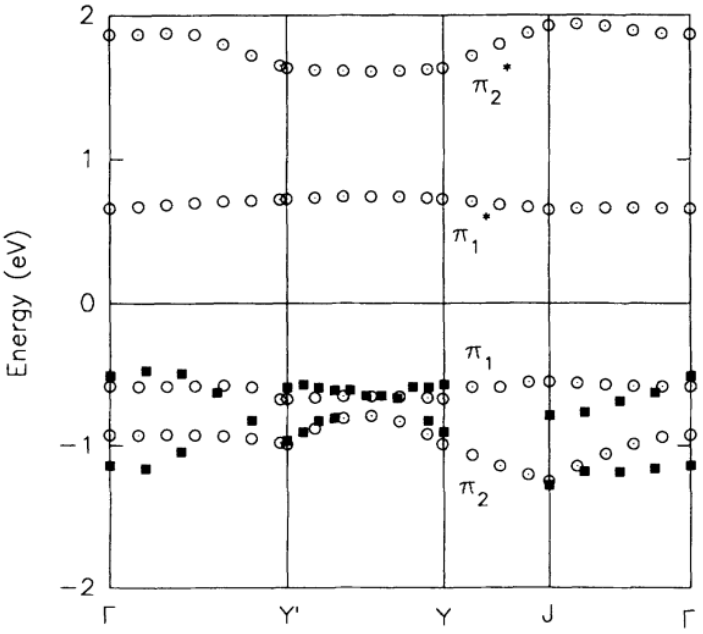

Figure 2.5: Band structure diagram displaying the dimer surface states computed by Low[11]. In circles the points calculated using tight-binding calculations, in squares experimental values. Adapted from Ref.[11]

2.6.3 Chemical Vapor Deposition of CaF_2 on Si(100)

CaF_2, or *fluorite* in its mineral form, is a crystal composed of ions of fluorine in simple cubic configuration, with calcium cations in the middle of the cubic sites of them. This compound is transparent to visible electromagnetic radiation and presents electronic optical absorption in the ultraviolet and lattice optical absorption in the infrared range[85]. Due to the presence of f-centers in the ionic lattice, the minerals of CaF_2 usually look colored, even tough the perfectly packed crystalline structure is transparent to visible spectra. The industrial use of this compound is wide: it is the main source of hydrofluoric acid[86], used for as cleaning chemical agent in metal smelting processes[87], has dental applications for enamel reconstruction and caries inhibition[88], The silicon-on-insulator (SOI), as we discussed before, demonstrate powerful features and potential applications to the design of epitaxial gate dielectrics, 3D integrated circuits mechanisms[89], and even the fabrication of logic and memory circuits immune to errors caused by α-particles popping out from high-energy cosmic rays events coming from outer space while interacting with the air molecules in our planet's atmosphere[90]. From the experimental point of view, the interface of CaF_2/Si(100) is generated by employing the Chemical Vapor Deposition (CVD) method. Hence, CaF_2 is obtained from fluorite crystals by evaporating them employing a graphite effusion cell. The temperature of this cell is kept around 1330 K during the evaporation process, and, for cooling down the crucible, water is used in order to optimize the temperature control[2]. The flux of the vapor containing the CaF_2 molecules is directed towards the silicon surface. The silicon surface to be used is chosen to have a relatively low number of defects, therefore it is analyzed inside the STM. For the epitaxial growth process, the bare Si(100) surface is then heated up to 1000 K using Joule heating. Due to the very close lattice match (0.6% difference) between the lattice constants of CaF2$_2$ and silicon crystal, and their similar fcc crystalline structure; the epitaxial growth is favorable for any direction[91].

The unit cell remaining after the deposition is expected to have at least one silicon dimer removed in an etching process.[2]. The chemical etching reaction mechanism for the first stage of CaF$_2$ deposition[92], because of the etched dimer, can be explained by the formation of SiF$_2$ species. But previous to the formation of this compound, the silicon surface requires to have a passivated silicon dimer, that can be explained by the initial reaction:

$$2\ \mathrm{Si} + \mathrm{CaF_2} \rightarrow \mathrm{Ca} + 2\ \mathrm{SiF},$$

but for etching completely the silicon dimer, at least 4 fluorine atoms will be needed, and thus 2 CaF$_2$ molecules. Therefore the next reaction is proposed[2]:

$$2\ \mathrm{Si} + 2\ \mathrm{CaF_2} \rightarrow \mathrm{Ca} + 2\ \mathrm{SiF} + \mathrm{CaF_2} \rightarrow 2\ \mathrm{Ca} + 2\ \mathrm{SiF_2}$$

Chapter 3

Methodology

In this section, the methodology is separated according to the followed construction sequence of the different supercells used for the simulations. The process of interface construction and structural relaxation is described, together with the steps for retrieving the converged parameters to be used for the DFT calculations. Core electrons are described with PAW potentials for Ca, F, H and Si atoms with the following configuration: Ca: [Ne] $3s^2$ $3p^6$ $4s^2$, F: [$1s^2$] $2s^2$ $2p^5$, H: $1s^2$ and Si [Ne] $3s^2$ $3p^2$; where the core electron configurations are within square brackets.

First, the convergence parameters such as cutoff energy and numbers in the *k*-point mesh, from the initial bulk structure are computed. Selecting the appropriate cutoff energy will ensure that the number of plane waves to simulate the material is large enough for keeping consistent results. After that, looking for the optimal cell volume is important for computing the total energies of our unit cell near the optimal value, and fit them to an EOS. This will allow us to extract important properties like the optimal crystal structure and the bulk modulus. Later, by having all the values optimized, the surface is constructed by repeating the unit cell accordingly and cleaving it into the desired direction.

Once the surface periodic supercell is appropriately constructed, different supercell sizes are chosen in order to have a proper surface reconstruction and reproduce the experimentally observed behavior. Subsequently, the first stage of CaF_2 deposition is set up and relaxed for later analysis of its electronic structure. Due to the slight degeneracy of the multiple possible combinations for the wetting layer configurations, the STM image simulations are used to distinguish them properly.

The following step is to reconstruct the atomic configuration of the stripe-like structures observed to form on top of the wetting layer[3]. Again, multiple configurations are selected as candidates and evaluated in function of the produced STM simulations. The proper structure to find has to present a non-zero band gap and similar STM image for demonstrating the accuracy of our proposed model.

3.1 Structural relaxation

3.1.1 Optimal parameters for bulk silicon crystal

The unit cell of the silicon crystal is well-known and can be found in multiple databases. The initial coordinates and lattice parameters are chosen close to the experimentally values in the scientific literature. The used unit cell of silicon is shown in Fig. 3.1 and was retrieved from *Materials Project*[93].

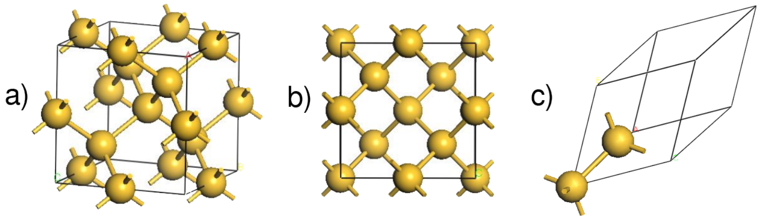

Figure 3.1: Crystal structure of fcc silicon used as initial input for our calculations. a) and b) display the unit cell with fcc diamond structure. c) Primitive cell of fcc silicon crystal, notice that the cell has two atoms. The black lines delimit the size of the cell and the Si atoms are represented by yellow spheres.

In order to find the optimal parameters, convergence tests are applied over the initial structure. First, the total energies of the structure for different values of cutoff energy are computed and compared until a convergency of 1< meV/atom is found, as shown in Fig. 3.2.

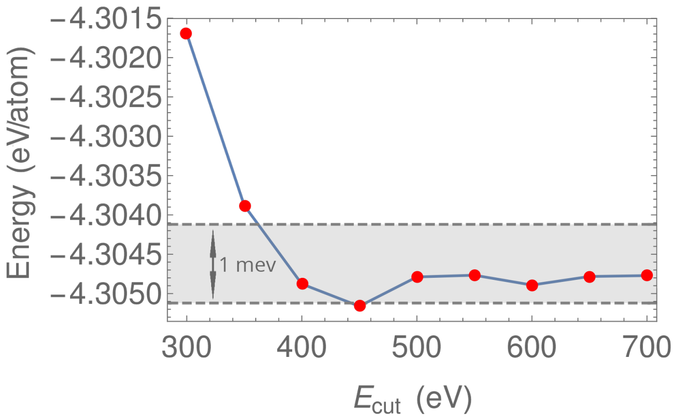

Figure 3.2: Convergency of the cutoff energy with respect to the total energies of the bulk structure; we observe convergency from $E_{\text{cut}} = 400$ eV.

Once the cutoff energy is stablished $E_{\text{cut}} = 400$ eV, a finite number of plane waves can be used to accurately describe the periodic wavefunctions of our material. After that, we can proceed to calculate the number of k-points to use in the calculations. The converged values can be observed to start to have a change in less than 1 meV/atom for a $9 \times 9 \times 9$ k-points mesh that is equivalent to a separation Δk of 0.035 Å^{-1} in the reciprocal space. The k-points grid is calculated using the Γ-centered Monkhorst-Pack method[38], implemented in VASP code.

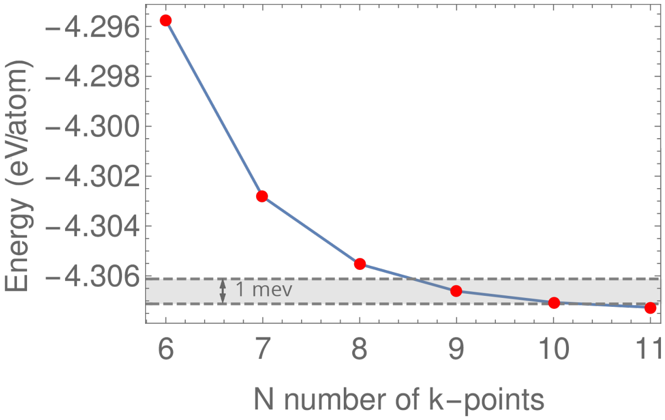

Figure 3.3: Convergence of the total energy with respect to the $N \times N \times N$ k-points grid; convergency is achieved from $N = 9$ and above.

After this convergency parameters are found, we can accurately find the optimal lattice constant of the bulk silicon structure. For this task, we fit the different values of the total energies obtained with respect to different lattice spacing values. The equation used for fitting this values is the equation of state (EOS) of Birch-Murnaghan[94], by considering the bulk modulus to be linearly related to a finite strain applied over a solid with respect to pressure[95]. Our EOS goes as follows:

$$E(V) = E_0 + \frac{9V_0B_0}{16}\left\{\left[\left(\frac{V_0}{V}\right)^{\frac{2}{3}} - 1\right]^3 B_0' + \left[6 - 4\left(\frac{V_0}{V}\right)^{\frac{2}{3}}\right]\right\} \tag{3.1}$$

Where the total energy depends on the volume V, and E_0, V_0, B_0, B_0' are the ground state energy, optimal volume, bulk modulus and the derivative of the bulk modulus respectively.

In order to fit the equation 3.1, we have to set it into the form:

$$E(V) = \alpha V^{-2} + \beta V^{-4/3} + \gamma V^{-2/3} + \delta \tag{3.2}$$

Hence, starting from the equation 3.1 we proceed to expand its terms:

$$E(V) = E_0 - \frac{9B_0V_0^3}{4V^2} - \frac{9}{16}B_0V_0B_0' + \frac{9}{16}B_0\left(\frac{V_0}{V}\right)^{2/3} B_0B_0' + \frac{63B_0\sqrt[3]{\frac{V_0}{V}}V_0^2}{8V} + \frac{27B_0V_0}{8V^{4/3}} - 9B_0\left(\frac{V_0}{V}\right)^{2/3} V_0 \tag{3.3}$$

Now, by further collecting the terms of similar order in V we find:

$$E(V) = E_0 + \frac{\frac{9}{16}B_0V_0^{5/3}B_0' - 9B_0V_0^{5/3}}{V^{2/3}} + \frac{63B_0V_0^{7/3}}{8V^{4/3}} - \frac{9B_0V_0^3}{4V^2} - \frac{9}{16}B_0V_0B_0^1 + \frac{27B_0V_0}{8} \tag{3.4}$$

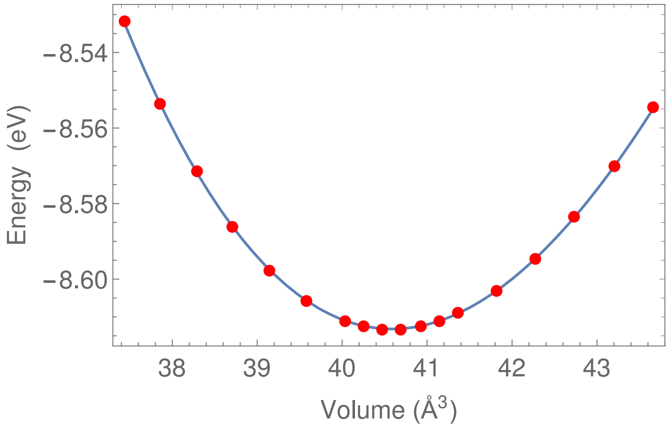

Figure 3.4: EOS for bulk Si, the red points are the computed optb86-vdW for a range of volumes and the blue line is the fitted EOS according to Eq. 3.1.

Therefore, the coefficients calculated after fitting the function with our computed data points are obtained and sumarized in Table 3.1.1.

Table 3.1: Values found after fitting the 3rd order EOS of Birch-Murnaghan[94]

Coefficient	Fitting Value	Coefficient	Fitting Value
$\alpha = -\frac{9B_0V_0^3}{4}$	9560.71 Å^6 keV	$\beta = \frac{63B_0V_0^{7/3}}{8}$	1214.32 Å^4 keV
$\gamma = \frac{9}{16}B_0V_0^{5/3}\left(-16 + B_0'\right)$	-411.264 Å$^{2/3}$ eV	$\delta = E_0 - \frac{9}{16}B_0V_0B_0' + \frac{27B_0V_0}{8}$	11.6997 eV

The fitted function now can be used to extract the bulk modulus, which is simply obtained from the relation expressed on equation 3.5 by considering the fact that the change in energy is given by $dE = -PdV$.

$$B_0 = -V\frac{\partial P}{\partial V} = V\frac{\partial^2 E}{\partial V^2}\bigg|_{V\rightarrow V_0} \tag{3.5}$$

The outcome of the vdW-DF calculations for the optimal structure of fcc-Si is summarized in Table 3.2.

Table 3.2: vdW-DF computed crystallographic data for optimal primitive cell of fcc-Si; here u, v and w are in fractional coordinates

Property		Calculated (optb86-vdW)	
Space group		$Fm\bar{3}m$	
$a = b = c$ (Å)		3.857	
$\alpha = \beta = \gamma$ (°)		60	
Volume (Å^3)		40.588	
B_0(GPa)		91.63	
Sites	u	v	w
Si	0.0	0.0	0.0

3.1.2 Si(100)-(1×1) and Si(100)-(2×1) surfaces

Starting from the optimized bulk crystal, the Si(100) surface is constructed. The unit cell of fcc-Si is cleaved by a (100) plane and repeated along the normal direction of the surface to get 8 atom layer thick; the Si atoms at bottom of the slab are passivated with H. The slabs are built with a 15 Å vacuum thickness to neglect the interactions between images along the z direction due to the periodic boundary conditions of the DFT VASP calculation. Finally, the Si-H bottom layer are frozen during relaxations to emulate the crystal structure of pristine fcc-Si. The schematic of the surface is depicted in Figure 3.5.

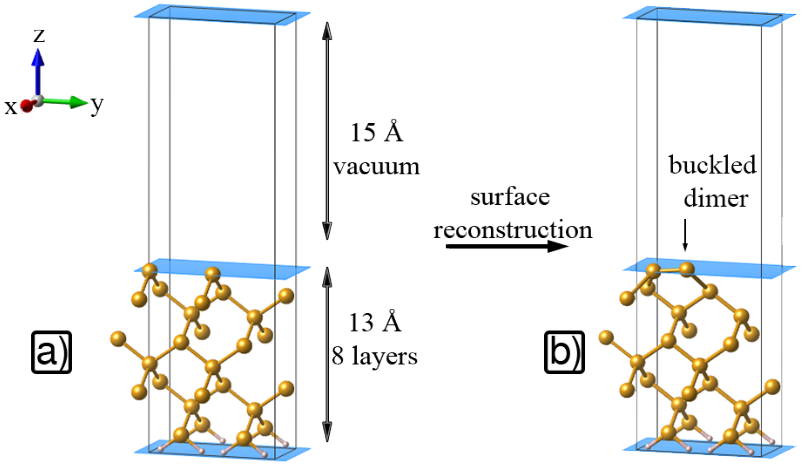

Figure 3.5: Atomic configuration of the Si(100) 2×1 surface (a) unrelaxed and (b) after relaxation. The slab has a 15 Åvacuum thickness along the z axis. The Si (H) atoms are represented by yellow (white) spheres and the box delimits the size of the supercell.

In order to include the buckling effect of the topmost silicon atoms that in nature appear after the cleaving of the surface as demonstrated experimentally[77], a surface of 2×1 is constructed and manipulated manually to allow a quicker relaxation. As described in the theoretical background, the topmost silicon atoms are moved closed to each other. Then, when its intermediate distance is enough for establishing a bond, one silicon is moved up, (towards $+z$ direction) and the other one down ($-z$ direction). Finally, a slight twist in the $[\bar{1}00]$ direction will leave the silicon atoms near the asymmetric dimer configuration. Then, the DFT calculation will draw the dimer spatial configuration towards its ground state configuration. The energy difference between dimer configuration is around 0.01 eV, therefore our convergence parameters are good enough to get an accurate result[78].

3.1.3 The CaF_2/Si(100) interface

For reconstructing the observed pattern on the STM images of the CaF_2/Si(100) interface, our supercell has to be repeated accordingly considering the observed motifs and buckling effect on the topmost silicon dimers. These details are important to correctly simulate the surface electronic structure.

Considering the fact that at least one silicon dimer is etched from the Si(100) 2×1 cell[2], for getting the wetting layer—the first stage of CaF_2 deposition—we use a 3×2 supercell where three Si dimers have to be considered. Consequently, by the proposed chemical etching reactions occurring on the surface during the CVD, the structure of the wetting layer is set as shown in Figure A.3. One dimer gets chemically bonded to fluorine atoms, the etched dimer vacancy allows the deposition of the calcium atom, and this leaves the new 3×2 supercell with one free dimer (*cf.* Figure A.3 (c,d))

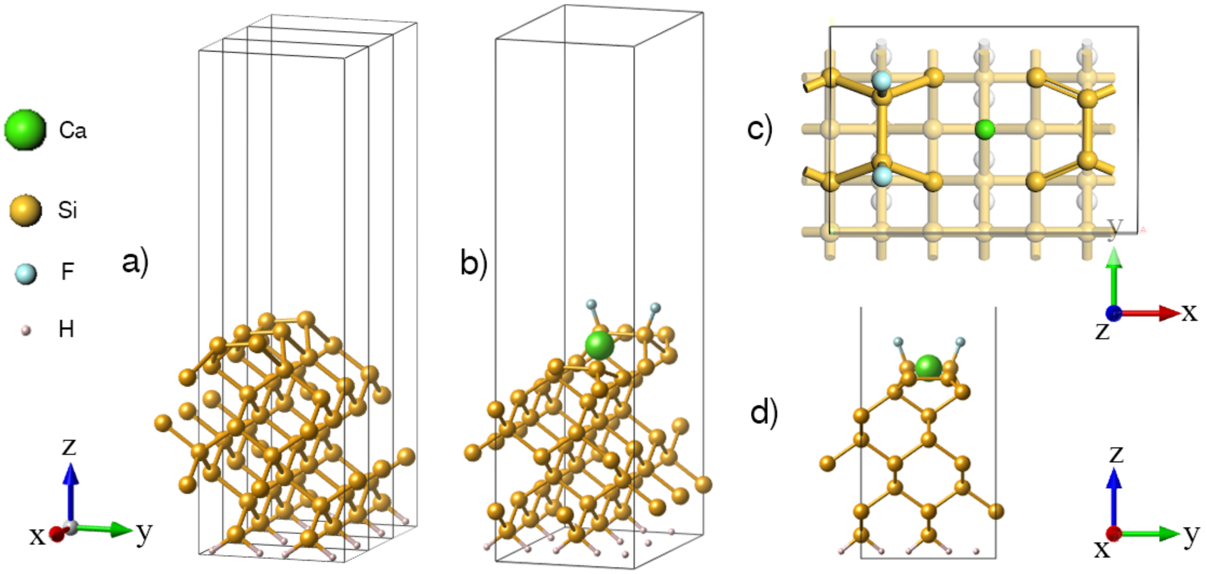

Figure 3.6: The diagram displays the proposed geometry of the interface. a) Si(100) 3×2 supercell; b) CaF_2/Si(100) overall view; c) Top view; the topmost silicon layer and CaF_2 is highlighted; d) Side view from the x direction

3.1.3.1 The wetting layer

Once the initial stage of deposition is prepared, to check what configuration resembles in a better way the experimental STM images, we have to consider a 3 × 4 surface supercell. This is due to the appearance of interspersed reversed 3 × 2 structures. Two settings can be distinguished, 3 × 4 'in-phase' configuration, composed of two parallel 3 × 2 constructions; and a 3 × 4 'out-of-phase', made of two antiparallel 3 × 2 cells. The experimental STM@7K image of the wetting layer by Chiaravalloti *et al.*[2] is shown in figure 3.7.

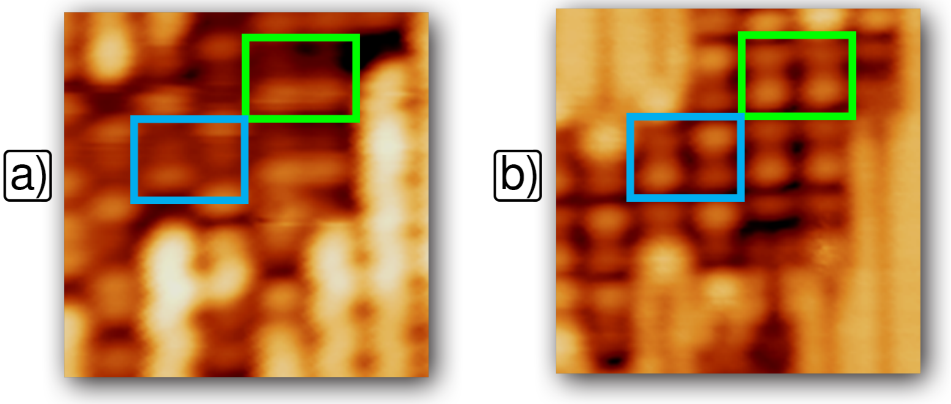

Figure 3.7: The experimentally measured STM image of the interface of interest. The 3 × 4 'in-phase' configuration is enclosed in green color, the 3 × 4 'out-of-phase' one in blue. a) Bias voltage of -1 V, occupied states. b) Bias voltage of +1 V, unoccupied states. Adapted from Ref.[2].

Interface nomenclature: As we have discussed, multiple interface atomic configurations can be associated to the pattern observed by STM experiment (*cf.* Fig. 3.7). Therefore, a clear nomenclature has to be specified to distinguish between the different possible arrangements of the ions in our interface supercell. All the possible combinations are shown in Figure 3.8.

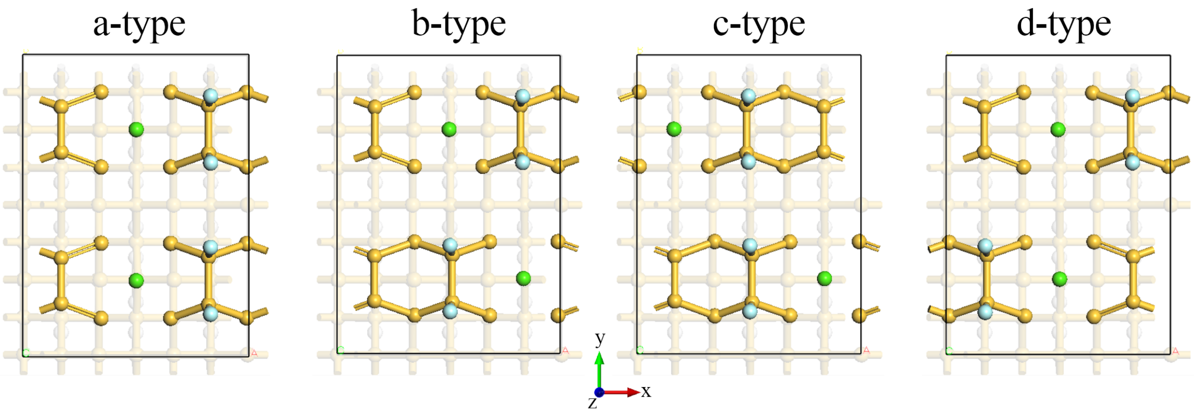

Figure 3.8: Proposed wetting layer atomic structures that may explain the experimental STM images as displayed in Fig. 3.7. The size of the surface supercell have approximately the same size that corresponds to a 3×4 supercell.

3.1.3.2 The stripe structure

The experimental STM image of the stripe structure is displayed in Fig. 3.9, it includes the WL and the bare Si(100) surface.

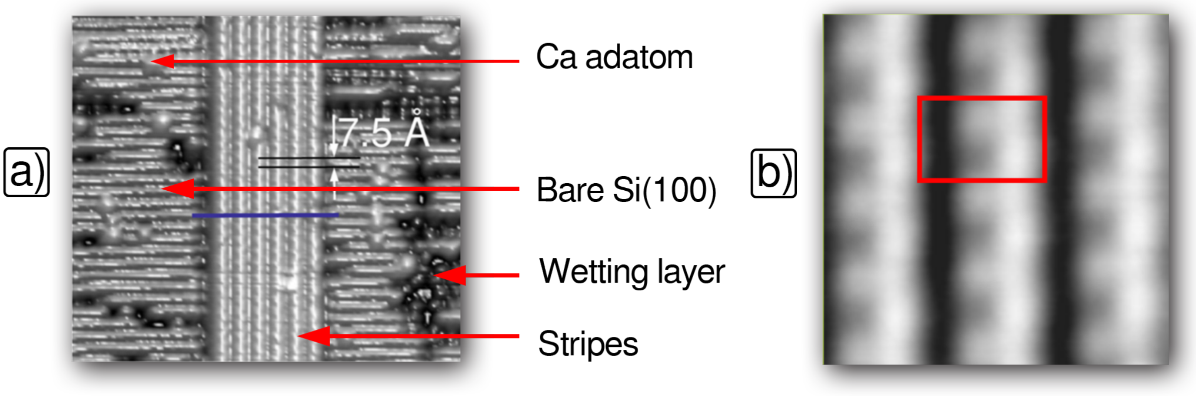

Figure 3.9: Occupied state STM topography of Si(100) with deposited CaF_2 (a) forming stripes, wetting layer and Ca adatoms. (b) High atomic resolution of the stripe atomic structure oriented along the y axis, notice the dented formation oriented along the x direction; the red box delimits the 3×4 supercell. These STM images were generated with $V_{\mathrm{BIAS}} = -2.5$V and tunneling current of 41 pA. Adapted from Ref. 2

Inspired on the experimental finding of Fig. 3.9, the next step is to get an accurate description of the stripe structure of the ultra-thin CaF_2/Si(100) interface. We need to reconstruct the epitaxial crystalline growth layer of the compound on top of the initial wetting layer of CaF_2/Si(100). The proposed stripe structure resembles a crystal of CaF_2 growing in its $[\bar{1}11]$ direction along the parallel free space in between silicon dimer rows. Two proposed configurations a-s1 and a-s2, based on the a-type structure (Fig. 3.8(a)); are displayed in the Figures 3.10 and 3.11, respectively.

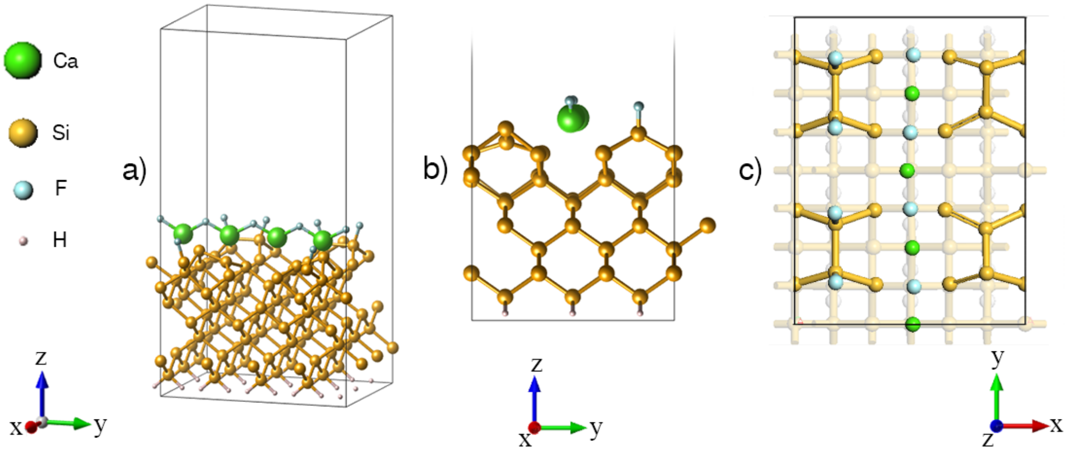

Figure 3.10: Atomic configuration of the proposed stripe model a-s1 based in the wetting layer model a-type from Fig. 3.8.

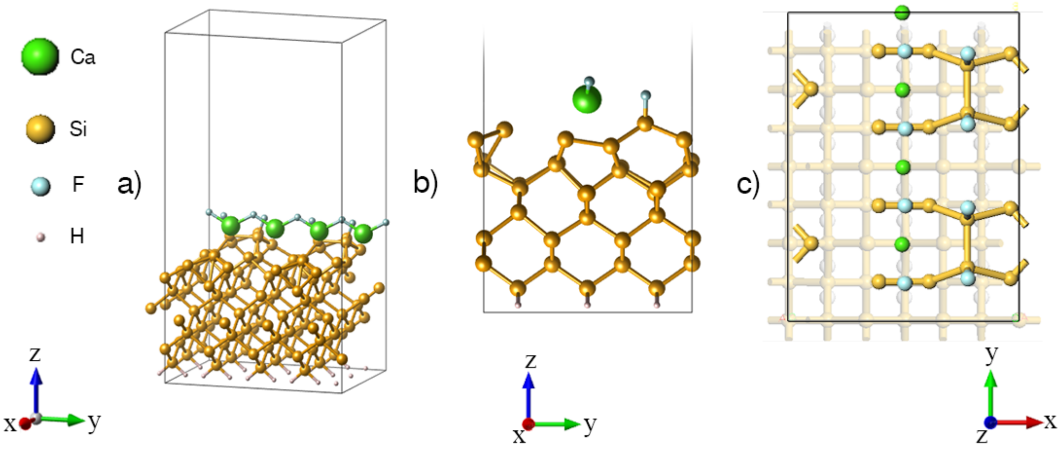

Figure 3.11: Atomic configuration of the proposed stripe model a-s2. This configuration can be clearly distinguished by the missing Si of one dimer row. This choice of construction is further discussed in the next chapter.

Chapter 4

Results & Discussion

The results of this thesis are divided into: the description of the electronic structure (DOS and PDOS) of the computed interfaces, and computed STM images of the previously optimized atomic configurations along the performed line-scans simulations for getting information about the topography of the interface. Then, the different computed results will be discussed, giving detail about the arguments in support of how and why we decided to select the achieved configurations as the ones we might find in the real experiment.

The convergency parameters and physically relevant values are summarized in Table 4

Table 4.1: optb86-vdW predicted structural and mechanical properties for bulk fcc-Si versus available experimental data.

Parameter	Calculated value(optb86-vdW)	Experimental Value
Lattice constant	5.455 Å	5.429 Å[81]
Bulk Modulus	91.63 GPa	95-105 GPa[81]
α=β=γ	90°	90°
Cell volume	162.351 Å^3	160.015 Å^3[79]

4.1 Electronic structure

The electronic structure will be analyzed by taking a look to the computed density of states (DOS) of the structures. Also, the partial density of states(PDOS) will give us information about how the different atomic species contribute to the overall electronic behavior of the material. With this data, we can compute important properties such as the band gap, from where we can tell if the material presents a band gap as observed experimentally.

4.1.1 Bulk silicon

The calculated DOS of the bulk silicon structure clearly suggests a semiconductor behavior. The zero along the x axis is set with respect to the Fermi level (Figure 4.1). The experimentally measured band gap of bulk silicon at 0 K is 1.17 eV[81], hence the error of the optb86-vdW functional is around around 43%, a typical limitation of DFT methods[96].

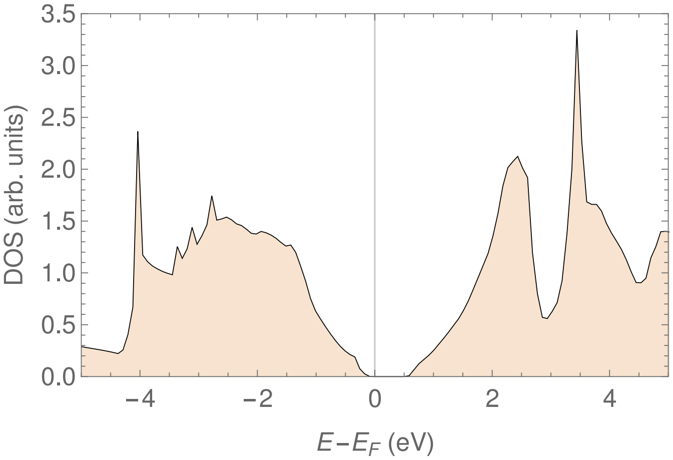

Figure 4.1: optb86-vdW computed DOS for optimal fcc-Si. We can observe a band gap of 0.55 eV

4.1.2 Si(100) 1×1, 2×1 and 2×2 surfaces

Taking in consideration the arguments of section 2.6.1, the correct electronic behavior of the Si(100) surface has to consider a 2×2 surface cell. By chosing this construction, a silicon buckled dimer will cause a band gap opening which will lower the total energy of the structure.

In figure 4.2 we can observe this expected semiconductor behavior of the Si(100) 2×1 and 2×2 surfaces, being the last the most stable. The main difference is the presence of metallic behavior of the 1×1 structure versus the small band gap of the 2×2 system. This due to a buckled dimer formation in 2×2 surface, it lowers the total energy with a bandgap opening of 0.206 eV (*cf.* Fig. 4.2 (c)).

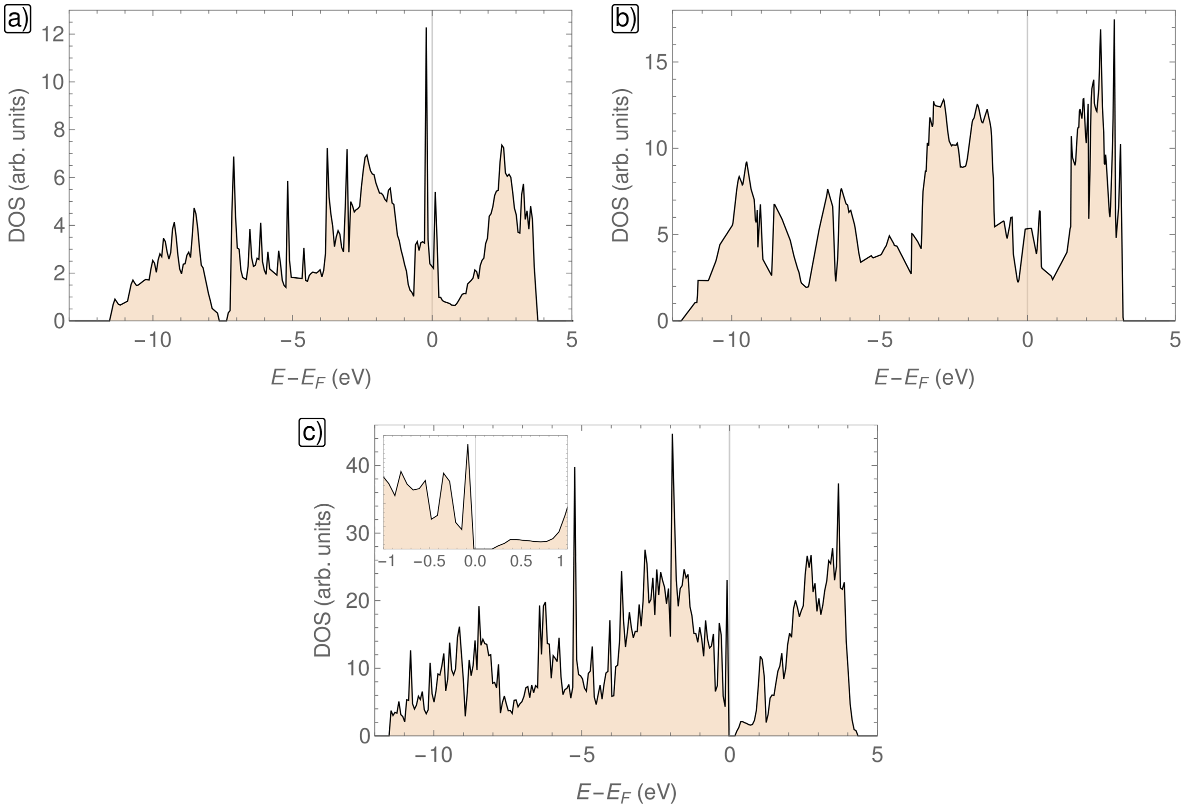

Figure 4.2: optb86-vdW computed DoS for (a) the Si(100) 1×1 surface, the lack of band gap suggest metallic behavior. (b) Si(100) 2×1 surface DoS (c) the Si(100) 2×2 surface displaying a bandgap opening of 0.206 eV. The graph is zoomed around the Fermi level for allowing a better visualization.

4.1.3 The CaF_2/Si(100) 3×2 wetting layer

First we consider the CaF_2/Si(100) 3×2 WL according to Ref.[2]. In that work, the atomic structure of the observed WL was solved with the CaF_2/Si(100) 3×2 (*cf.* Fig.6 in Ref.[2]). If that structure is repeated along y axis we get the CaF_2/Si(100) 3×4 a-type supercell as displayed in Fig. 3.8. The computed electronic structure for CaF_2/Si(100) 3×2 WL is displayed in Fig. A.3. We computed the PDOS for each sublayer. The WL shows a tiny electronic states below the Fermi level E_F. On the conduction band, at E_F, we observe only Ca-3p states closing the bandgap of the pristine Si(100). The L1 layers, composed of the buckling dimer, is separated into two layers: L1a and L1b, those contain the topmost and downshifted dimer respectively. We can observe that the downshifted silicon atom gives a bigger contribution to states near the Fermi energy on the conduction band. As we go deeper into the bulk along z, the PDOS become closer to the bulk structure as expected.

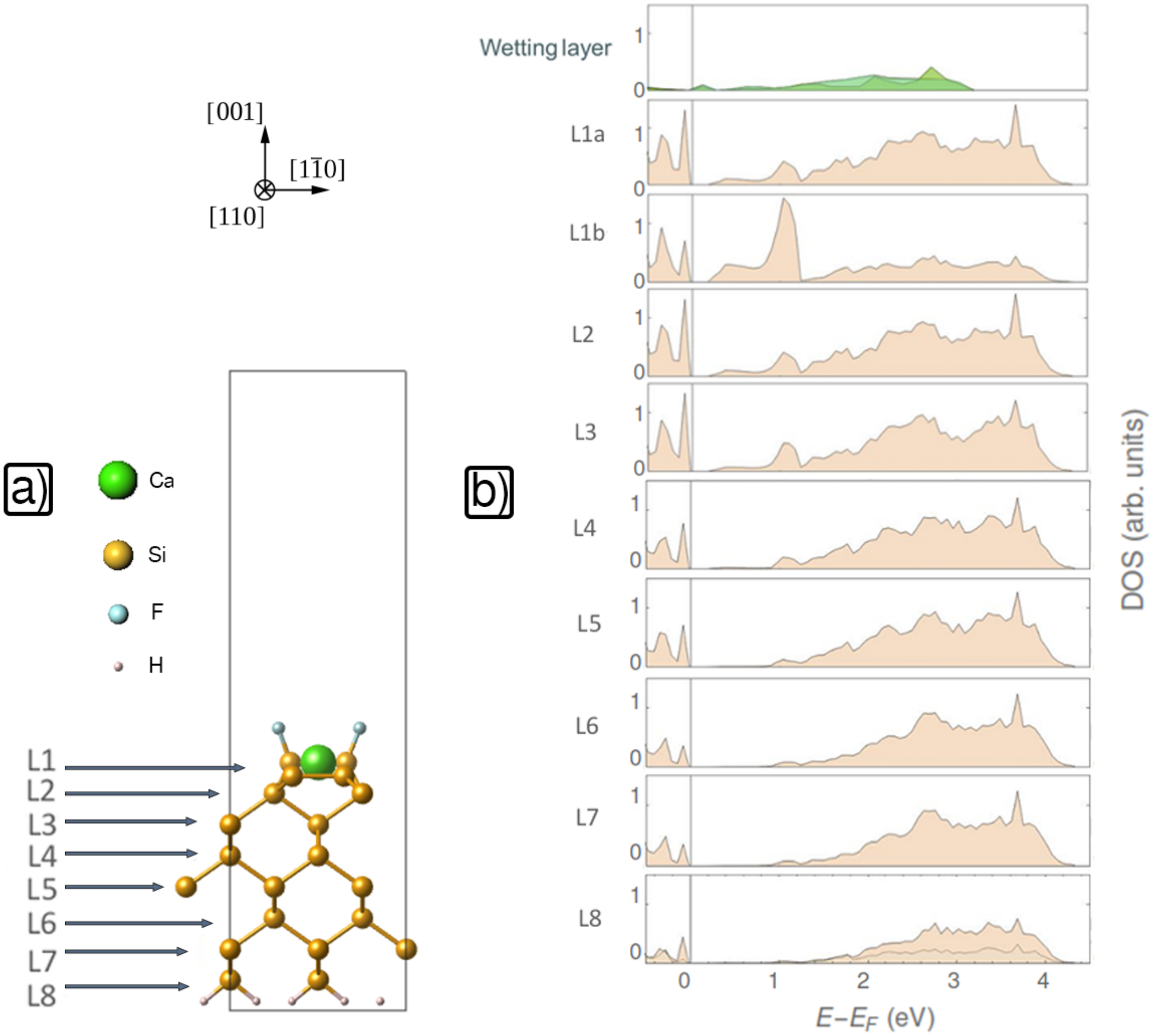

Figure 4.3: optb86-vdW computed PDOS by layers of the CaF_2/Si(100) 3 × 2 structure, (a) side view in the x direction is shown (b) PDOS for each layer.

4.1.3.1 STM simulation

After getting our fully relaxed structure and a DOS that replicates the already reported results for the atomic and electronic structure of the WL in Ref. 2. The computed STM images and line scans for our computed $CaF_2/Si(100)$ 3×2 interface are displayed in Fig. 4.4. Certainly, the $CaF_2/Si(100)$ 3×4 type-a reproduces the same images as we expected. For the corresponding images for type-b, -c and -d, please refer to Appendix A.

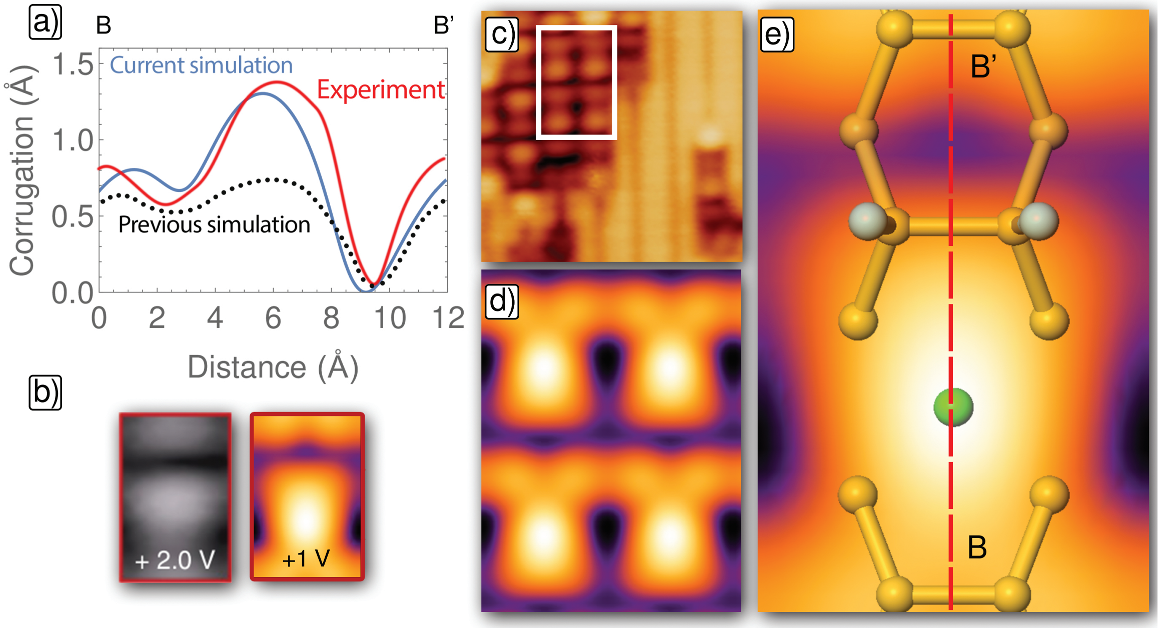

Figure 4.4: STM images for unoccupied states, theory versus experiment. (a) Line scans along BB' showing the computed (blue line) and experimental (red line); the black dotted line represents the reported simulation by Chiaravalloti *et al.*[2]. (b) Experimental STM of WL (V_{BIAS} = +2V) versus the simulated STM (V_{BIAS} = +2V); the red rectangle delimits the 3×2 supercell. (c) Experimental unoccupied states STM image of the $CaF_2/Si(100)$ interface where WL and bare Si(100) are visible. (d) Simulated STM image expanded along x and y directions that replicates the area enclosed by the white rectangle in (c). (e) Close-up of simulated STM image in (b). Calcium, Fluorine and Silicon atoms are colored in green, gray and yellow spheres, respectively. Experimental images are adapted from Ref. 2.

In Fig. 4.4(a), the line-scans are obtained from the simulated STM images for he $CaF_2/Si(100)$ 3x2 supercell displayed in Fig. 4.4(b) and (d). From the line-scan simulation we can clearly observe a better improvement on the predicted corrugation considering previous PBE simulations as reported by Chiaravalloti *et al.*[2]. Considering the STM images in Fig 4.4, the brightest sites of the image are related to the Ca-3p states that protrude into the vacuum while the secondary bright sites are related to the location of the surface Si-dimer due to their Si-2p states. Finally, the darkest sites are located in between the Si-F and the surface Si-dimer site (*cf.*, Fig. 4.4(e)). To stress the good prediction of the computed structure, notice the WL island of CaF_2/Si(100) enclosed by the white rectangle of the experimental image in Fig. 4.4(c) that is satisfactorily reproduced in the computed STM image in Fig. 4.4(d).

The same analysis is performed for negative bias voltages (occupied states) STM images as displayed in Figure 4.5. The simulated line-scan got also improved versus the previously reported study[2] (Figure 4.5(a)), this result strength the reliability of the model as well as the vdW-DF applied. The experimental STM image for the occupied states is nicely reproduced by our simulation (*cf.* Figure 4.5(b)). The brightest sites of the STM are located above the Si-dimer, mainly due to their protruding $2p_z$ orbitals remaining after the dimerization. The silicon atom in the bulk is bonded to 4 neighboring, but in the dimer, the silicon atoms have only 3 bonds, then the extra dangling bond protrudes in the z direction (for a clearer description, refer to figure 2.3). The secondary bright sites are located around the Ca and Si-F region and related to a contribution of Ca-3p + F-$2p_y$ + Si-3p states. Finally, the darkest site is located between the Ca and the nearest Si-dimer (See Figure 4.5(e) for high definition image). In addition, Figure 4.5(c) and (d) shows a nice agreement between experiment and theory. These results complement the results for unoccupied states STM and suggest the improvements of the optb86-vdW functional over the former PBE simulations when applied to the CaF_2/Si(100) interfaces.

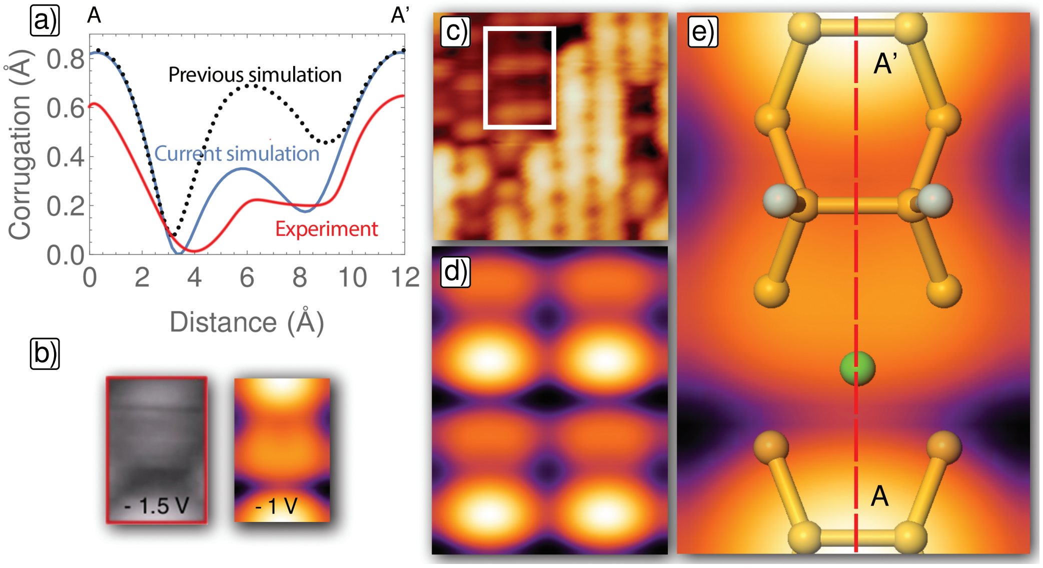

Figure 4.5: STM images for occupied states, theory versus experiment. (a) Line scans along AA' showing the computed (blue line) and experimental (red line); the black dotted line represents the reported simulation by Chiaravalloti *et al.*[2]. (b) Experimental STM of WL ($V_{\mathrm{BIAS}} = -1.5$V) versus the simulated STM ($V_{\mathrm{BIAS}} = -1$V); the red rectangle delimits the 3×2 supercell. (c) Experimental occupied states STM image of the CaF_2/Si(100) interface where WL and bare Si(100) are visible. (d) Simulated STM image expanded along x and y directions that replicates the area enclosed by the white rectangle in (c). (e) Close-up of simulated STM image in (b). Calcium, Fluorine and Silicon atoms are colored in green, gray and yellow spheres, respectively. Experimental images are adapted from Ref. 2

Contrary to the previous STM measurement, the calcium ion on top of the etched silicon dimer demonstrates a shorter amount of occupied states, thus those zones are less shiny. The silicon dimers present the highest brightness, mainly due to their protruding p_z orbitals remaining after the dimerization. The silicon atom in the bulk is bonded to 4 neighboring, but in the dimer, the silicon atoms have just 3 bonds, then the extra dangling bond protrudes in the z direction (for a clearer description, refer to figure 2.3).

4.1.4 The CaF_2/Si(100) 3×4 wetting layer

Despite the detailed description of the WL atomic structure by the work of Chiaravalloti *et al.*[2], we noticed that their experimental STM images not only 3×2 structures are observed—as highlighted by the white rectangle in Figures 4.4c and 4.5c; but also inverted 3×4 reconstructions highlighted by the green rectangle in Fig. 4.6(b) and (d). The parallel formations outside the patched regions in the experimental STM image are patterns related to the bare Si(100). It can be noted that in Figure 4.6(d), the dimers are described by bright spots, thus outside the WL islands, bare silicon is observed. Among the 3×4 structures proposed (Fig. 3.8), the d-type was the structure that reproduces best the inverted patterns appearing on the experimental STM images for the WL. The STM calculations are observed to reproduce qualitatively the same motiffs observed in the real material, see Fig. 4.6.

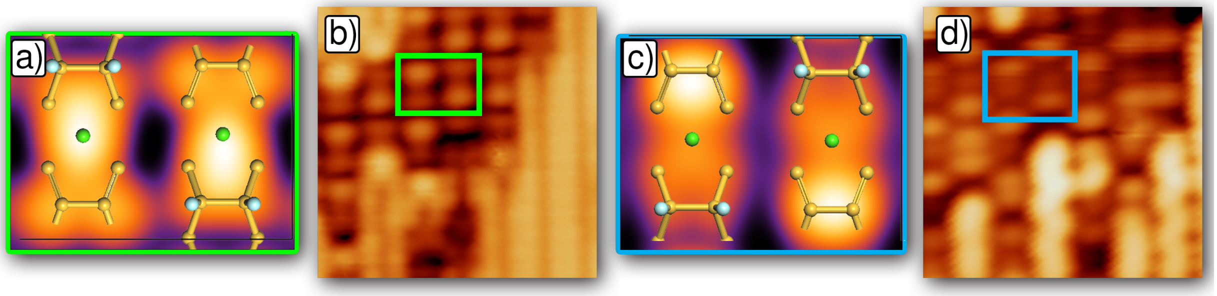

Figure 4.6: STM images where out-of-phase 3×4 pattern is discussed. (a) Computed unoccupied state STM image of the d-type structure, $V_{\mathrm{BIAS}} = +1$V. (b) Experimental unoccupied state STM image, $V_{\mathrm{BIAS}} = +2$V, the green rectangle highlight the 'out-of-phase' pattern. (c) Computed occupied state STM image of d-type structure ($V_{\mathrm{BIAS}} = -1$V) versus the (d) experimental occupied state STM image, $V_{\mathrm{BIAS}} = -1.5$V; in this case, the blue rectangle highlight the 'out-of-phase' pattern. All the experimental STM images are adapted from Ref. 2.

4.1.5 Solving the stripe structure

Considering the satisfactory results of either the a-type and d-type structure structures that best describe the observed STM images, we proceed to consider the formation of the stripe structure reported in Ref. 3. Since both theoretical structures are basically the flip of the Si-F units, we guessed that a-type has all the principal features needed as the starting structure. In the work of Chiaravalloti *et al.*[3], they observed the stripe configuration to have a linear atomic formation perpendicular to the silicon dimer rows. Then, as we discussed before, the Ca and F atoms were organized in a similar manner as if they recrystallized along the [111] direction of a typical CaF_2 crystal.

Before we describe the proposed interfaces for solving the stripe structure, we have to bear in mind two main features: i. The stripe has to be symmetrical only along the y direction within the 3×4 supercell; this reasoning is based on the experimental STM image displayed in Fig. 3.9 that shows a 3×2 reconstruction. ii. The measured scanning tunneling spectroscopy (STS) probed on the stripe region report the system to have bigger bandgap than the bare Si(100)[3] as displayed in Fig. 4.7, then our proposed structure should present wider bandgap in comparison to the bandgap of pristine Si(100). Following that reasoning, we propose two likely interfaces: the S1 (Fig. 4.8(a)) and the S2 (Fig. 4.9(a)) structures; the results of the simulations are described in the following sections.

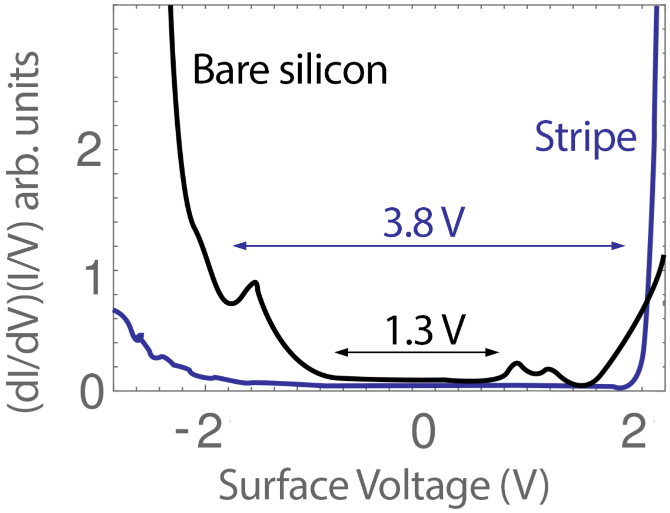

Figure 4.7: Experimental STS signal dI/dV for the bare Si(100) (black line), and the stripe structure (blue line). This experiment shows the bandgap of the different systems studied here. Adapted from Ref. 3.

The computed results of total energies depicted in the table 4.1.5 cannot be used to distinguish the most stable configuration, given the very small energy differences. The total energies per atom (a,b,c,d -type structures have 122 atoms each) differ in less than 1 meV, which accordingly to our convergence parameters criteria, go beyond our employed computational precision.

Table 4.2: Computed total energies for the a,b,c,d -types. Also, the difference in height of the specific structural units with respect to the Si dimer Δz is detailed.

	a-type	b-type	c-type	d-type
Computed total Energy	-617.6885 eV	-617.7228 eV	-617.7103 eV	-617.7170 eV
	-5.06302 (eV/atom)	-5.06330 (eV/atom)	-5.06319 (eV/atom)	-5.06325 (eV/atom)
Si-F Δz (w.r.t. Si atom)	+0.488 Å	+0.408 Å	+0.488 Å	+0.468 Å
Ca Δz	+0.502 Å	+0.625 Å	+0.612 Å	+0.593 Å

4.1.5.1 The S1 stripe structure

Before we proceed to describe the results for the S1 structure, it is important to mention that we tried to explore different metastable configurations of this structure by manipulating the Si-dimer "by hands" and allowing full relaxation. For all the atempts performed, in all the cases the final relaxed structure was the one displayed in Fig. 4.8(a). The computed electronic structure of the fully relaxed S1 structure is displayed in Fig. 4.8. The S1 system does not reproduce the expected band gap as reported by Chiaravalloti *et al.*[2] (*cf.* Figs 4.8(b-c) and Fig. 4.7), the system present a metallic state. Interestingly, the simulated STM image for the occupied state shows close similarities with the experiment.

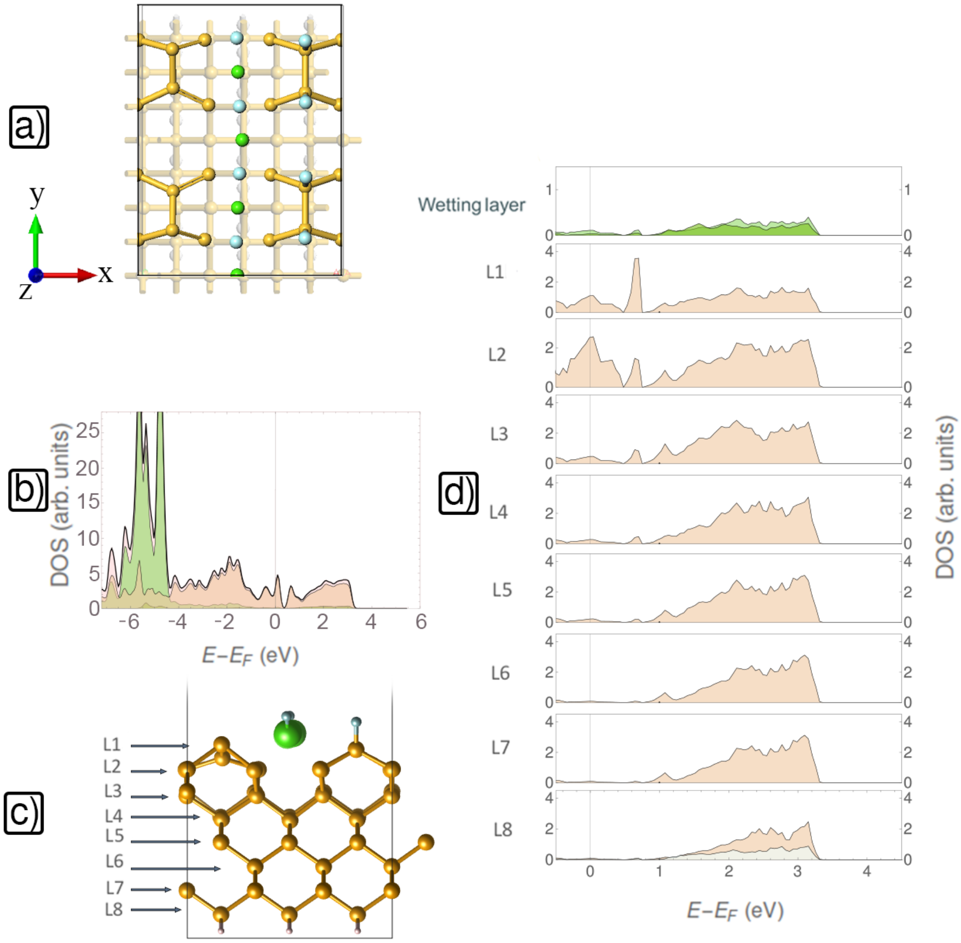

Figure 4.8: Computed atomic and electronic structure for S1 stripe model, (a) Relaxed atomic structure, (b) Total DOS of slab, (c) PDOS for each layer and (d) Simulated unoccupied STM image for $V_{\mathrm{BIAS}} = -1$V.

4.1.5.2 The S2 stripe structure

By analyzing what atomic species contribute to the apparition of states around the Fermi energy of the S1 structure (Fig. 4.8), the contributions are observed to come from the Si-2p_x+ 2p_z orbitals of the silicon dimers at the surface. In order to get rid of those levels, one silicon atom is removed from the dimer, assuming it can be also be etched during the deposition process of CaF_2. After constructing and relaxing that S2 structure, depicted on Figure 4.9(a), a band gap opening of 0.88 eV appears. Therefore, the missing silicon atom on the prevoiusly formed dimer causes the remaining Si-2p_x+ 2p_z protruding orbitals to become more energetic (with respect to the S1 configuration), thus shifting those unnocupied states towards the conduction band and opening widening the gap. Taking a look at the simulated STM images for negative bias, dark areas around the remaining single silicon atom can be observed, suggesting absences of occupied states over those species. By the other hand, the brightest zones appear to be around the CaF_2 crystalline stripe formation, thus meaning abundant occupied states under the Fermi Level of the material. The chemically bonded fluorine atoms do not present many states at those energies too, but the weak signal comming out from this zones reconstruct the dented structure observed in the experiment (check fig. 4.10).

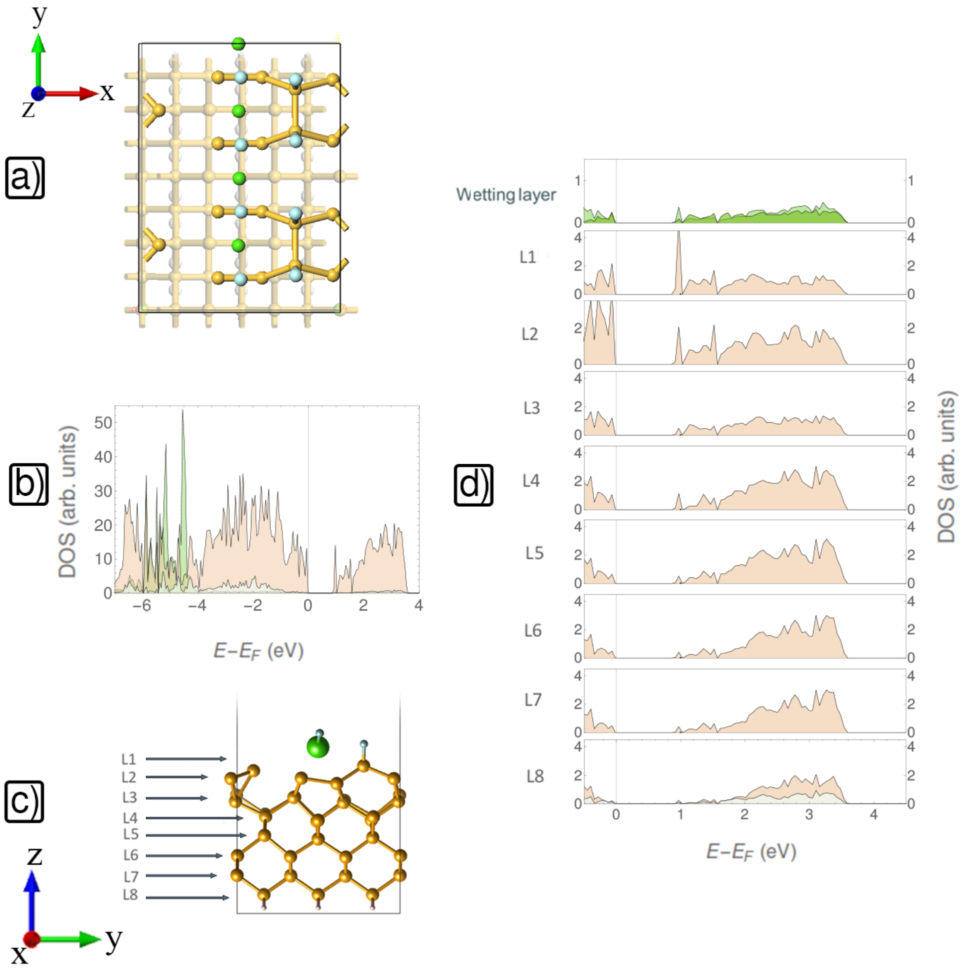

Figure 4.9: Computed atomic and electronic structure for S2 stripe model, (a) Relaxed atomic structure and Simulated unoccupied STM image for $V_{\mathrm{BIAS}} = -1\mathrm{V}$, (b) Total DOS of slab, (c) PDOS for each layer, notice the bandgap opening of 0.88 eV.

Table 4.1.5.2 summarizes the calculated band gaps from the proposed models and compares it to the experimental STS results. It is important to bear in mind that our DFT calculations have limitations in predicting the actual values of the bandgap but it is important to stress that at least the computed values keep the experimental trend, i.e., the bandgap of the stripe is bigger than the bare Si(100) in accordance with the experiment.

Table 4.3: Comparison between the computed versus experimental band gaps as reported in Ref. 3.

	Bare Si(100)	CaF_2/Si(100) stripe	$E_{gap,stripe}/E_{gap,bare}$
optb86-vdW	0.206 eV	0.878 eV	~3
Experiment	1.3 eV	3.8 eV	~4

4.1.5.3 S2 model that solve the observed stripe topology

After computing the STM images for both structures S1 and S2, it can be noted that those structures show similar STM pattern. Therefore, analyzing the electronic structure via their PDOS became the ultimate criteria for choosing an accurate answer to the problem of the atomic structure of the CaF_2/Si(100) stripe formation.

A summary of the computed occupied states STM images of proposed stripe configurations versus the corresponding experimental STM image are displayed in Figure 4.10(a-b). For the structure S1, the silicon dimers are observed to contribute more to occupied states, and the CaF_2 linear layer to form the parallel stripe structures (Fig. 4.10(c)). On the other hand, the S2 structure—that has semiconductor character in agreement with the experiment—demonstrates brighter zones along the CaF_2 columns and the dented pattern is given by the Si-F dimers generating a pattern that resembles better the experimental STM.

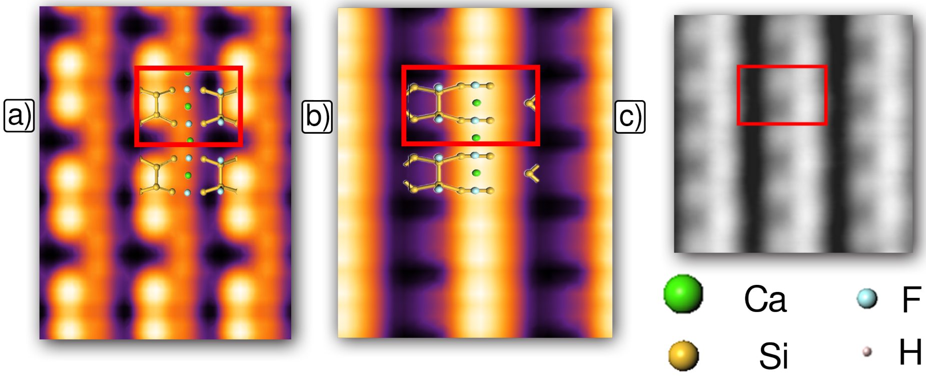

Figure 4.10: The simulated occupied state STM images for the (a) S1 and (b) S2 are compared directly to (c) the experimental STM.

Chapter 5

Conclusions & Outlook

In this work, we have performed a DFT calculation within the vdW-DF approximation in order to solve the atomic and electronic structure of the CaF_2/Si(100) interface.

In the first stage we calculated the wetting layer of this interface. Different configurations for the 3×2 and 3×4 wetting layer reconstructions were proposed, relaxed and analyzed. From the computed electronic structure, we simulated the STM images of the considered geometries. The results shows that 3×4 a-(aligned) and d-(reversed) types demonstrated to resemble the observed patterns of the experimental measurements. Moreover, the line-scans for measuring the surface topology depicted a qualitatively accurate description of the experimental data for the wetting layer geometries.

Considering the nice agreement between our vdW-DF calculations with the experimental data on the wetting layer, the 'stripe'-like structures were constructed. The systems were fully relaxed and their atomic and eletronic structure were computed including the simulation of the corresponding STM images. At this stage, our proposed stripe-like structures exhibited similar STM patterns between each other and the experimemt. However, the actual structure that explains the experiment should also present a bandgap opening as observed on the STS experiments. Taking this in consideration, we can compare the computed PDOS with the STS. The a-s2 structure depicted in the figure 4.9 presented a non-zero band gap vs. the metallic a-s1 stripe structure. Therefore, it is presented here as a solution to the exact atomic description of the CaF_2 stripe-like formation on top of Si(100) surfaces.

The electronic structure analysis has shown that the band gap values are still far away from the experimentally measured ones, mainly due to the fact that semi-local DFT functionals tend to understimate this value[96]. Extra adjustments have to be considered to get an accurate description of the band gap of the material.

The use of a functional with an adequate van der Waals kernel to describe the non-local dispersion interactions was found to be very important in this kind of systems, specially due to the physisorbed atoms where this dispersion becomes important. Thanks to this functional, we were able to reproduce and greatly improve previously reported results in the scientific literature.

Appendix A

Long Appendix 1 Heading

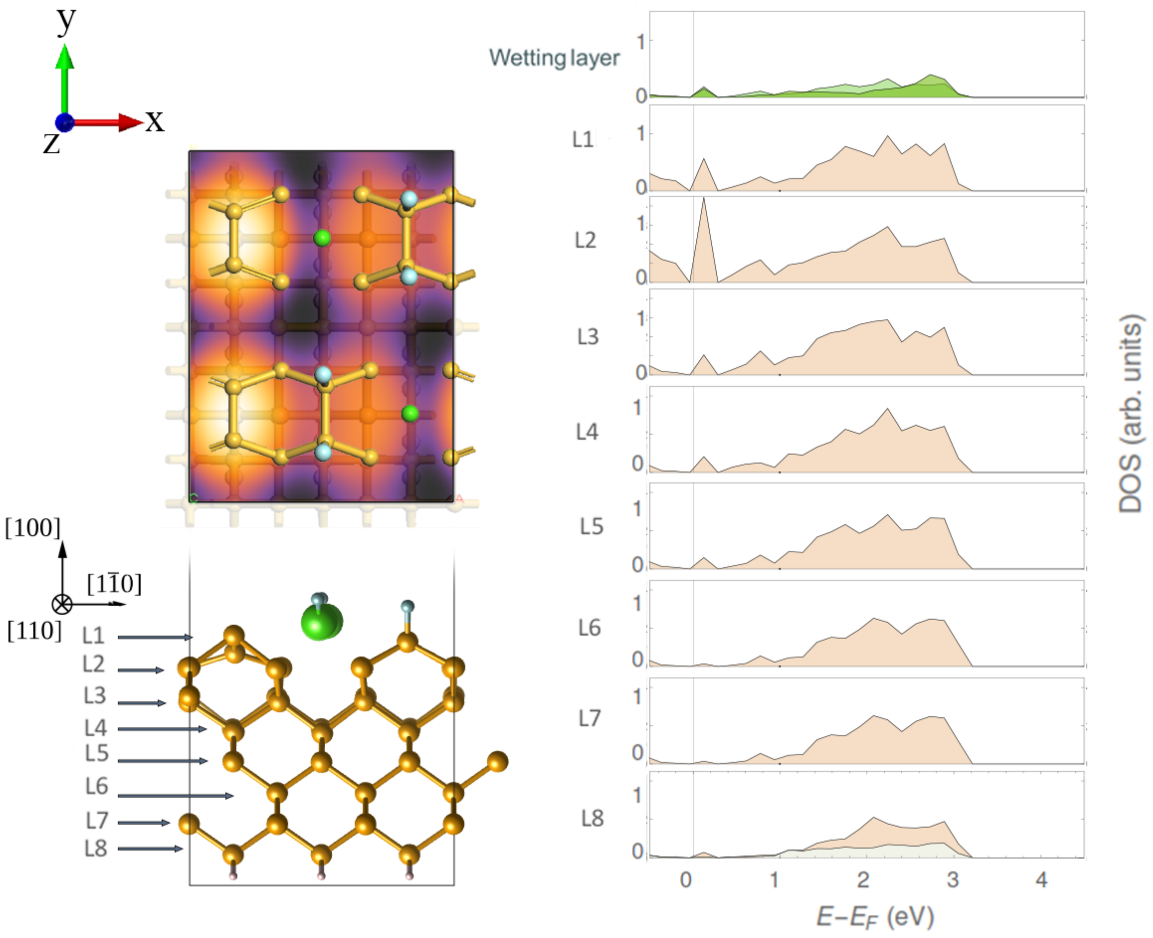

Figure A.1: PDOS by layers of the b-type structure, a side view in the x direction is shown, along with the PDoS of each layer. The STM simulation presented here was calculated at $V_{\mathrm{BIAS}} = -1V$

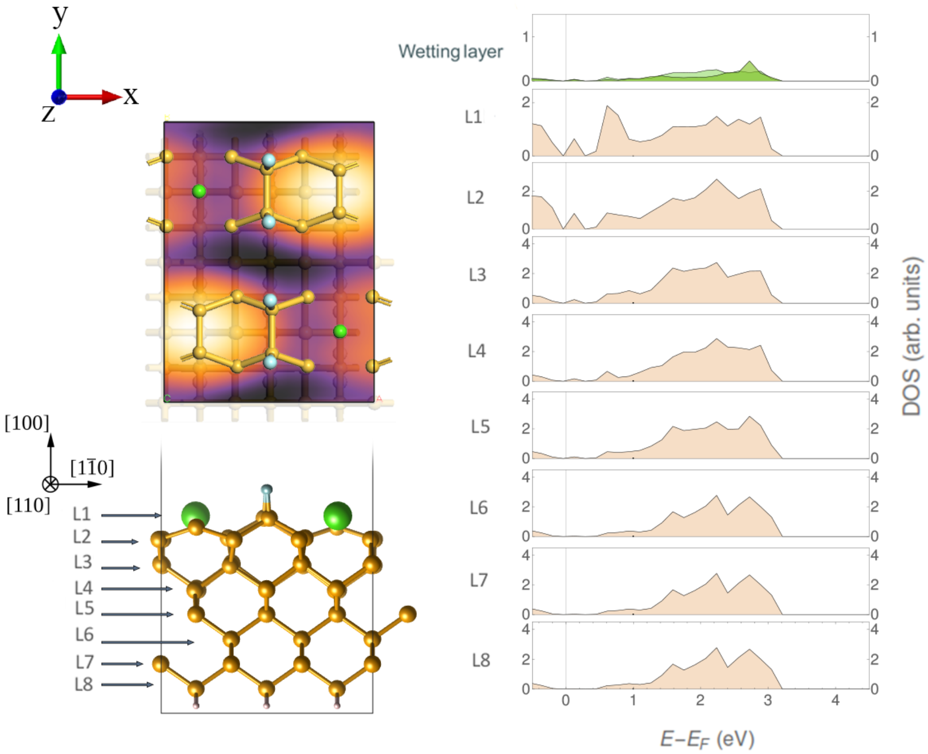

Figure A.2: Partial Density of States separated by layers of the c-type structure, a side view in the x direction is shown, along with the PDoS of each layer. STM image at $V_{\text{BIAS}} = -1V$

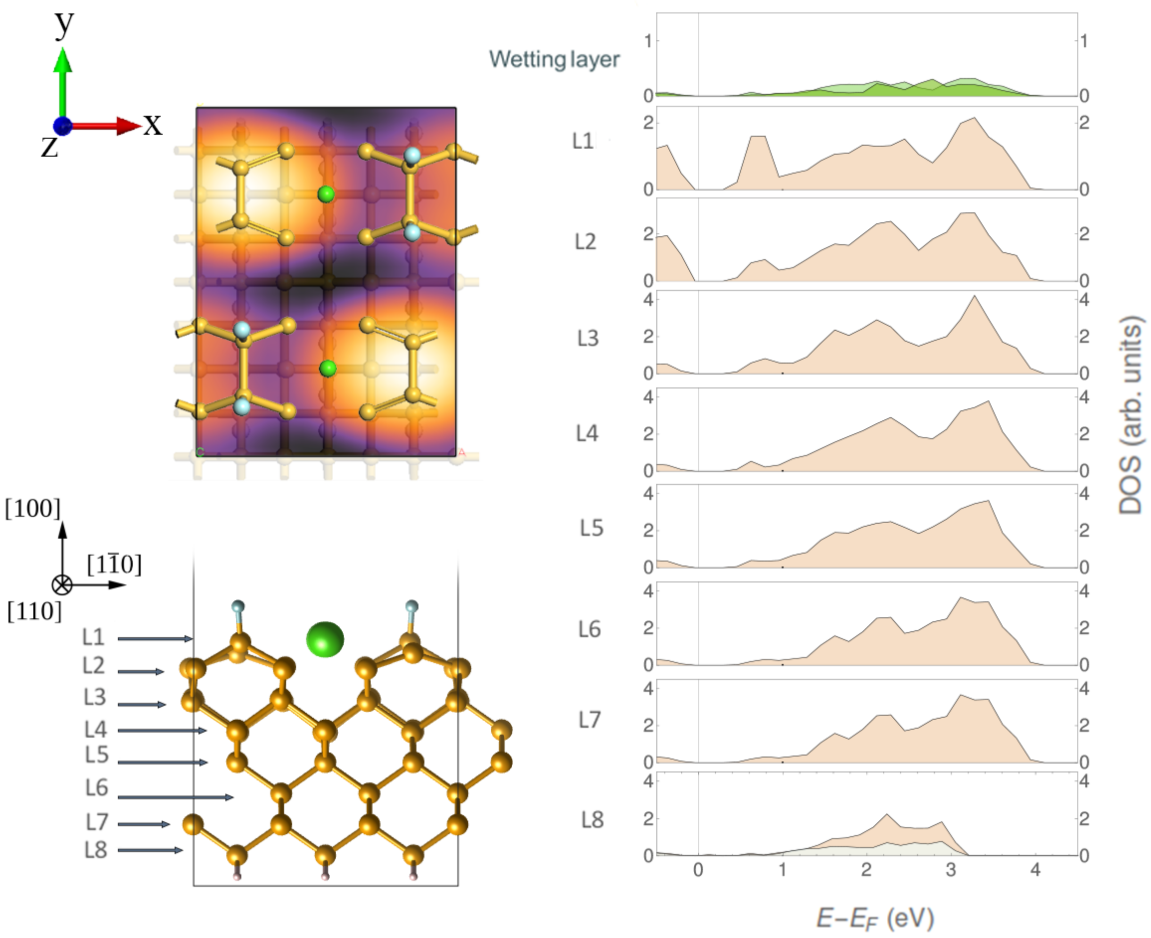

Figure A.3: PDOS by layers of the d-type structure, different views are displayed for structure visualization. STM image at $V_{\text{BIAS}} = -1V$

Bibliography

[1] Colton, R. J. Nanoscale measurements and manipulation. *Journal of Vacuum Science and Technology B: Microelectronics and Nanometer Structures* **2004**, *22*, 1609–1635.

[2] Chiaravalloti, F.; Dujardin, G.; Riedel, D.; Pinto, H. P.; Foster, A. S. Atomic-scale study of the adsorption of calcium fluoride on Si(100) at low-coverage regime. *Physical Review B - Condensed Matter and Materials Physics* **2011**, *84*, 1–7.

[3] Chiaravalloti, F.; Dujardin, G.; Riedel, D. Atomic scale control of hexaphenyl molecules manipulation along functionalized ultra-thin insulating layer on the Si(1 0 0) surface at low temperature (9K). *Journal of Physics Condensed Matter* **2015**, *27*, 1DUMY.

[4] Rydberg, H.; Dion, M.; Jacobson, N.; Schröder, E.; Hyldgaard, P.; Simak, S. I.; Langreth, D. C.; Lundqvist, B. I. Van der waals density functional for layered structures. *Physical Review Letters* **2003**, *91*, 1–4.

[5] McClellan iii, J. E.; Dorn, H. *Science and technology in world history: an introduction*; JHU Press, 2015.

[6] Goodell, B.; Xie, X.; Qian, Y.; Daniel, G.; Peterson, M.; Jellison, J. Carbon nanotubes produced from natural cellulosic materials. *Journal of nanoscience and nanotechnology* **2008**, *8*, 2472–2474.

[7] Reibold, M.; Paufler, P.; Levin, A.; Kochmann, W.; Pätzke, N.; Meyer, D. Carbon nanotubes in an ancient Damascus sabre. *Nature* **2006**, *444*, 286–286.

[8] Vexler, M.; Illarionov, Y. Y.; Suturin, S.; Fedorov, V.; Sokolov, N. Tunneling of electrons with conservation of the transverse wave vector in the Au/CaF 2/Si (111) system. *Physics of the Solid State* **2010**, *52*, 2357–2363.

[9] Rieger, D.; Himpsel, F.; Karlsson, U. O.; McFeely, F.; Morar, J.; Yarmoff, J. Electronic structure of the CaF 2/Si (111) interface. *Physical Review B* **1986**, *34*, 7295.

[10] Sokolov, N.; Suturin, S. MBE growth of calcium and cadmium fluoride nanostructures on silicon. *Applied surface science* **2001**, *175*, 619–628.

[11] Low, K.; Ong, C. Electronic structure of the Si (100) c (4× 2) and p (2× 2) surfaces. *Physical Review B* **1994**, *50*, 5352.

[12] Toton, D.; Lorenz, C. D.; Rompotis, N.; Martsinovich, N.; Kantorovich, L. Temperature control in molecular dynamic simulations of non-equilibrium processes. *Journal of Physics: Condensed Matter* **2010**, *22*, 074205.

[13] David Scholl, *Electronic Structure*; 2012; pp 119–134.

[14] Schrödinger, E. An undulatory theory of the mechanics of atoms and molecules. *Physical review* **1926**, *28*, 1049.

[15] Griffiths, D. J.; Schroeter, D. F. *Introduction to quantum mechanics*; Cambridge University Press, 2018.

[16] Giustino, F. *Materials modelling using density functional theory: properties and predictions*; Oxford University Press, 2014.

[17] Mattuck, R. D. *A guide to Feynman diagrams in the many-body problem*; Courier Corporation, 1992.

[18] Born, M.; Oppenheimer, R. Zur quantentheorie der molekeln. *Annalen der physik* **1927**, *389*, 457–484.

[19] Martin, R. M.; Martin, R. M. *Electronic structure: basic theory and practical methods*; Cambridge university press, 2004.

[20] Born, M.; Huang, K. *Dynamical theory of crystal lattices*; Clarendon press, 1954.

[21] Aschroft, N.; Mermin, N. Solid State Physics. Thomson Learning. 1976.

[22] Heine, V.; Weaire, D. Solid State Physics, ed. H. Ehrenreich, F. Seitz and D. Turnbull. *Academic Press, New York* **1970**, *24*, 249.

[23] Hellmann, H. A new approximation method in the problem of many electrons. *The Journal of Chemical Physics* **1935**, *3*, 61–61.

[24] Hellmann, H.; Kassatotschkin, W. Metallic binding according to the combined approximation procedure. *The Journal of Chemical Physics* **1936**, *4*, 324–325.

[25] Harrison, W. A. Pseudopotentials in the Theory of Metals. *1966, 336 P. W. A. BENJAMIN, INC., NEW YORK* **1966**,

[26] Zunger, A.; Cohen, M. L. Density-functional pseudopotential approach to crystal phase stability and electronic structure. *Physical Review Letters* **1978**, *41*, 53.

[27] Hamann, D.; Schlüter, M.; Chiang, C. Norm-conserving pseudopotentials. *Physical Review Letters* **1979**, *43*, 1494.

[28] Vanderbilt, D. Optimally smooth norm-conserving pseudopotentials. *Physical Review B* **1985**, *32*, 8412.

[29] Garrity, K. F.; Bennett, J. W.; Rabe, K. M.; Vanderbilt, D. Pseudopotentials for high-throughput DFT calculations. *Computational Materials Science* **2014**, *81*, 446–452.

[30] Blöchl, P. E. Projector augmented-wave method. *Physical review B* **1994**, *50*, 17953.

[31] Vanderbilt, D. Soft self-consistent pseudopotentials in a generalized eigenvalue formalism. *Phys. Rev. B* **1990**, *41*, 7892–7895.

[32] Kantorovich, L. *Quantum theory of the solid state: an introduction*; Springer Science & Business Media, 2004; Vol. 136.

[33] Hohenberg, P.; Kohn, W. Inhomogeneous electron gas. *Physical review* **1964**, *136*, B864.

[34] Levy, M.; Nagy, Á. Variational density-functional theory for an individual excited state. *Physical review letters* **1999**, *83*, 4361.

[35] Bartolotti, L. J. Time-dependent Kohn-Sham density-functional theory. *Physical Review A* **1982**, *26*, 2243.

[36] Kohn, W.; Sham, L. J. Self-consistent equations including exchange and correlation effects. *Physical review* **1965**, *140*, A1133.

[37] Bloch, F. Quantum mechanics of electrons in crystal lattices. *Z. Phys* **1928**, *52*, 555–600.

[38] Monkhorst, H. J.; Pack, J. D. Special points for Brillouin-zone integrations. *Physical review B* **1976**, *13*, 5188.

[39] Burke, K. The abc of dft. *Department of Chemistry, University of California* **2007**, 40.

[40] Engel, E.; Dreizler, R. M. *Density functional theory*; Springer, 2013.

[41] Jones, R. O.; Gunnarsson, O. The density functional formalism, its applications and prospects. *Reviews of Modern Physics* **1989**, *61*, 689.

[42] Umemoto, K.; Wentzcovitch, R. M.; Allen, P. B. Dissociation of MgSiO3 in the cores of gas giants and terrestrial exoplanets. *Science* **2006**, *311*, 983–986.

[43] Herman, F.; Van Dyke, J. P.; Ortenburger, I. B. Improved statistical exchange approximation for inhomogeneous many-electron systems. *Physical Review Letters* **1969**, *22*, 807.

[44] Rydberg, H.; Dion, M.; Jacobson, N.; Schröder, E.; Hyldgaard, P.; Simak, S.; Langreth, D. C.; Lundqvist, B. I. Van der Waals density functional for layered structures. *Physical review letters* **2003**, *91*, 126402.

[45] Dion, M.; Rydberg, H.; Schröder, E.; Langreth, D. C.; Lundqvist, B. I. Van der Waals density functional for general geometries. *Physical review letters* **2004**, *92*, 246401.

[46] Berland, K.; Cooper, V. R.; Lee, K.; Schröder, E.; Thonhauser, T.; Hyldgaard, P.; Lundqvist, B. I. van der Waals forces in density functional theory: a review of the vdW-DF method. *Reports on Progress in Physics* **2015**, *78*, 066501.

[47] Klimeš, J.; Bowler, D. R.; Michaelides, A. Chemical accuracy for the van der Waals density functional. *Journal of Physics: Condensed Matter* **2009**, *22*, 022201.

[48] Vydrov, O. A.; Van Voorhis, T. Nonlocal van der Waals density functional made simple. *Physical review letters* **2009**, *103*, 063004.

[49] Klimeš, J.; Bowler, D. R.; Michaelides, A. Van der Waals density functionals applied to solids. *Physical Review B* **2011**, *83*, 195131.

[50] Gest, H. The discovery of microorganisms by Robert Hooke and Antoni Van Leeuwenhoek, fellows of the Royal Society. *Notes and records of the Royal Society of London* **2004**, *58*, 187–201.

[51] Ruska, E. The development of the electron microscope and of electron microscopy. *Reviews of modern physics* **1987**, *59*, 627.

[52] Amano, Y.; Díaz, L. Introducción a la microscopía electrónica. *Principios, Aplicaciones. Guayaquil: Panamericana* **2012**,

[53] Chen, C. J. *Introduction to scanning tunneling microscopy*; Oxford University Press on Demand, 1993; Vol. 4.

[54] Morita, S. *Roadmap of scanning probe microscopy*; Springer Science & Business Media, 2006.

[55] Harrison, W. *Electronic structure and the properties of solids: the physics of the chemical bond*; Dover Books on Physics; Dover Publications, 1989.

[56] Hehre, W. J.; Stewart, R. F.; Pople, J. A. self-consistent molecular-orbital methods. i. use of gaussian expansions of Slater-type atomic orbitals. *The Journal of Chemical Physics* **1969**, *51*, 2657–2664.

[57] Pople, J. A.; Binkley, J. S.; Seeger, R. Theoretical models incorporating electron correlation. *International Journal of Quantum Chemistry* **1976**, *10*, 1–19.

[58] Krishnan, R.; Binkley, J. S.; Seeger, R.; Pople, J. A. Self-consistent molecular orbital methods. XX. A basis set for correlated wave functions. *The Journal of chemical physics* **1980**, *72*, 650–654.

[59] Hafner, J. Materials simulations using VASP—a quantum perspective to materials science. *Computer physics communications* **2007**, *177*, 6–13.

[60] Paier, J.; Hirschl, R.; Marsman, M.; Kresse, G. The Perdew–Burke–Ernzerhof exchange-correlation functional applied to the G2-1 test set using a plane-wave basis set. *The Journal of chemical physics* **2005**, *122*, 234102.

[61] Feynman, R. P. Forces in molecules. *Physical review* **1939**, *56*, 340.

[62] Deaven, D. M.; Ho, K.-M. Molecular geometry optimization with a genetic algorithm. *Physical review letters* **1995**, *75*, 288.

[63] others,, *et al.* The atomic simulation environment—a Python library for working with atoms. *Journal of Physics: Condensed Matter* **2017**, *29*, 273002.

[64] Dubois, P. F. Making applications programmable. *Computers in Physics* **1994**, *8*, 70–73.

[65] Bahn, S. R.; Jacobsen, K. W. An object-oriented scripting interface to a legacy electronic structure code. *Computing in Science & Engineering* **2002**, *4*, 56–66.

[66] Cameron, A. G. Abundances of the elements in the solar system. *Space Science Reviews* **1973**, *15*, 121–146.

[67] de Lavoisier, A.; Cuchet, G. *Traité élémentaire de chimie: présenté dans un ordre nouveau et d'après les découvertes modernes ...*; Traité élémentaire de chimie: présenté dans un ordre nouveau et d'après les découvertes modernes; Chez Cuchet, 1789.

[68] Gay-Lussac, J.; Thénard, L. *Recherches physico-chimiques: faites sur la pile, sur la préparation chimique et les propriétés du potassium et du sodium, sur la décomposition de l'acide boracique, sur les acides fluorique, muriatique et muriatique oxigéné, sur l'action chimique de la lumière, sur l'analyse végétale et animale, etc*; Recherches physico-chimiques v. 1; Deterville, 1811.

[69] vetenskapsakademien, K. S. *Kongl. vetenskaps academiens handlingar*; Landmarks II: Journals v. 12; Lars Salvius, 1824.

[70] Bose, J. C. Detector for electrical disturbances. 1904; US Patent 755,840.

[71] Black, L. E. *New perspectives on surface passivation: Understanding the Si-Al2O3 interface*; Springer, 2016.

[72] others,, *et al. Silicon surfaces and formation of interfaces: basic science in the industrial world*; World Scientific, 2000.

[73] Riedel, D.; Lastapis, M.; Martin, M.; Dujardin, G. Influence of tip-surface interactions and surface defects on Si (100) surface structures by low-temperature (5 K) scanning tunneling microscopy. *Physical Review B* **2004**, *69*, 121301.

[74] Schlier, R.; Farnsworth, H. Structure and adsorption characteristics of clean surfaces of germanium and silicon. *The Journal of Chemical Physics* **1959**, *30*, 917–926.

[75] Wolkow, R. A. Direct observation of an increase in buckled dimers on Si (001) at low temperature. *Physical review letters* **1992**, *68*, 2636.

[76] Luca, G.; Betti, M. G.; Carlo, M.; Shkrebtii, A.; Del Sole, R.; Cepek, C.; Goldoni, A.; Modesti, S. Dynamics of the Si (100) surface. **1997**,

[77] Chadi, D. Si (100) surfaces: Atomic and electronic structures. *Journal of Vacuum Science and Technology* **1979**, *16*, 1290–1296.

[78] Pomyalov, A. Relaxation of the adsorption geometry of Sb and K on Si (001) surface induced by an electric field. *Physical Review B* **1998**, *57*, 8989.

[79] Eranna, G. *Crystal Growth and Evaluation of Silicon for VLSI and ULSI*; CRC Press, 2014.

[80] Kittel, C. *Introduction to Solid State Physics Global ed*; Wiley: Hoboken, NJ, 2018.

[81] Batchelder, D.; Simmons, R. Lattice constants and thermal expansivities of silicon and of calcium fluoride between 6 and 322 K. *The Journal of Chemical Physics* **1964**, *41*, 2324–2329.

[82] Kentsch, C.; Kutschera, M.; Weinelt, M.; Fauster, T.; Rohlfing, M. Electronic structure of Si (100) surfaces studied by two-photon photoemission. *Physical Review B* **2001**, *65*, 035323.

[83] Dąbrowski, J.; Scheffler, M. Self-consistent study of the electronic and structural properties of the clean Si (001)(2× 1) surface. *Applied surface science* **1992**, *56*, 15–19.

[84] Northrup, J. E. Electronic structure of Si (100) c (4× 2) calculated within the GW approximation. *Physical Review B* **1993**, *47*, 10032.

[85] Brown, F. C. *The physics of solids: ionic crystals, lattice vibrations, and imperfections*; WA Benjamin, 1967.

[86] Aigueperse, J.; Mollard, P.; Devilliers, D.; Chemla, M.; Faron, R.; Romano, R.; Cuer, J. P. Fluorine compounds, inorganic. *Ullmann's encyclopedia of industrial chemistry* **2000**,

[87] Senning, A. *Elsevier's Dictionary of Chemoetymology: The Whys and Whences of Chemical Nomenclature and Terminology*; Elsevier, 2006.

[88] Rølla, G.; Saxegaard, E. Critical evaluation of the composition and use of topical fluorides, with emphasis on the role of calcium fluoride in caries inhibition. *Journal of dental research* **1990**, *69*, 780–785.

[89] Schowalter, L.; Fathauer, R.; Goehner, R.; Turner, L.; DeBlois, R.; Hashimoto, S.; Peng, J.-L.; Gibson, W.; Krusius, J. Epitaxial growth and characterization of CaF2 on Si. *Journal of applied physics* **1985**, *58*, 302–308.

[90] Benac, M. J.; Cowley, A. H.; Jones, R. A.; Tasch Jr, A. F. Growth of polycrystalline calcium fluoride via low-temperature organometallic chemical vapor deposition. *Chemistry of Materials* **1989**, *1*, 289–290.

[91] Asano, T.; Ishiwara, H. Epitaxial growth of Si films on CaF2/Si structures with thin Si layers predeposited at room temperature. *Journal of applied physics* **1984**, *55*, 3566–3570.

[92] Flamm, D. L. Mechanisms of silicon etching in fluorine-and chlorine-containing plasmas. *Pure and Applied Chemistry* **1990**, *62*, 1709–1720.

[93] Ceder, G.; Persson, K. The Materials Project: A Materials Genome Approach. 2010.

[94] Murnaghan, F. D. The Compressibility of Media under Extreme Pressures. *Proceedings of the National Academy of Sciences* **1944**, *30*, 244–247.

[95] Tyuterev, V.; Vast, N. Murnaghan's equation of state for the electronic ground state energy. *Computational materials science* **2006**, *38*, 350–353.

[96] Chan, M.; Ceder, G. Efficient band gap prediction for solids. *Physical review letters* **2010**, *105*, 196403.